COLUMBIA-125
Fermilab Library
0 1160 0010907 8

Report No. 125
DOE/ER/40669-1
UC-414

Columbia University
in the City of New York

Acceleration of Electrons Using an Inverse Free Electron Laser Auto-Accelerator

Iddo K. Wernick and Thomas C. Marshall

July 1992

FERMILAB
SEP 1992
LIBRARY
ROUTE TO
NAME

Work Supported by DE-FG02-91ER40669

Plasma Physics Laboratory
Department of Applied Physics
School of Engineering and Applied Science
Columbia University
New York, New York 10027

ACCELERATION OF ELECTRONS USING AN INVERSE FREE ELECTRON LASER AUTO-ACCELERATOR

Iddo K. Wernick and Thomas C. Marshall

COLUMBIA UNIVERSITY

1992

ABSTRACT

ACCELERATION OF ELECTRONS USING AN INVERSE FREE ELECTRON LASER AUTO-ACCELERATOR

Iddo K. Wernick and Thomas C. Marshall

We present data from our study of a device known as the inverse free electron laser [IFEL]. First, numerical simulations were performed to optimize the design parameters for an experiment that accelerates electrons in the presence of an undulator by stimulated absorption of radiation. The Columbia free electron laser [FEL] was configured as an auto-accelerator [IFELA] system [V=750keV, I=200A]; high power [MW's] FEL radiation at ~1.65mm is developed along the first section of an undulator [41cm long, period 1.43cm, field 600G] inside a quasi-optical resonator. The electron beam then traverses a second section of undulator [38cm long, period tapered from 1.8-2.25cm, field 400-480G] where a fraction of the electrons is accelerated by stimulated absorption of the 1.65mm wavelength power developed in the first undulator section. The second undulator section has very low gain and does not generate power on its own. We have found that as much as 60% of the power generated in the first section can be absorbed in the second section, providing that the initial electron energy is chosen correctly with respect to the parameters chosen for the first and second undulators. An electron momentum spectrometer is used to monitor the distribution of electron energies as the electrons exit the IFELA.

We have found; using our experimental parameters, that roughly 10% of the electrons are accelerated to energies as high as 1100 keV, in accordance with predictions from the numerical model. The appearance of high energy electrons is correlated with the abrupt absorption of millimeter power. The autoaccelerator configuration is used because there is no intense source of coherent power at the 1.65mm design wavelength other than the FEL. Also included are the numerical simulation results for an advanced version of an advanced IFEL experiment [Initial energy 50MeV, Final energy ~100MeV, Laser power ~10^{12}W].

TABLE OF CONTENTS

Chapter 1 **INTRODUCTION**

1.1 Introduction

1.2 The FEL

1.3 The IFEL

1.4 The IFELA

Chapter 2 **IFEL THEORY**

2.1 Introduction

2.2 FEL equations

2.3 Conditions imposed on FEL equations to insure acceleration

2.4 Numerical simulation results

2.5 Stimulated Emission/absorption in the undulator

2.6 An analytical expression for a tapering parameter while varying only $\lambda_w(z)$

Chapter 3 **EXPERIMENTAL APPARATUS**

3.1 Introduction

3.2 Marx capacitor bank

3.3 Transmission line and vacuum diode

3.4 Main solenoid

3.5 Laser Resonator

3.6 Diagnostics

Chapter 4 **IFELA EXPERIMENTAL SETUP**

4.1 Two stage reverse tapered undulator

4.2 Magneto-optic electron transport and magnetic spectrometer

4.3 Detection of C'erenkov light produced by spatially resolved energetic electrons

4.4 Calibration and energy resolution for the mass spectrometer/optical detection system

Chapter 5 **DATA COLLECTION**

5.1 Preliminary experimental findings

5.2 Overview of data collection

5.3 Sample data

5.4 Data selection and interpretation

Chapter 6 **RESULTS**

6.1 Radiation data

6.2 Electron energy data

Chapter 7 **AN IFEL ACCELERATOR TEST DEMONSTRATION**

7.1 Introduction

7.2 A model for an IFEL accelerator

7.3 Simulation results

7.4 Conclusions

References

CHAPTER 1

1.1 INTRODUCTION

The term "Free Electron Laser" [FEL] was coined by Madey[1] in 1977 to describe a device he had operated which generated infrared[10.6,3.4μm] wavelength radiation from a relativistic electron beam which passed though an undulator (a device that supplies a periodic transverse magnetostatic field) contained within an optical resonator[2]. However, FEL physics dates back to work done by Motz and Nakamura[3] in 1959 with undulators. Also predating Madey's experiment was a paper that appeared in 1972 by Palmer[4] which examined the possibility of using stimulated absorption to accelerate electrons in an undulator in the presence of high power laser radiation. The concept described by Palmer was later given the name "the inverse free electron laser" [IFEL]. In the IFEL energy drawn from a high intensity laser beam increases the kinetic energy of electrons by stimulated absorption, the inverse of what occurs by stimulated emission in an FEL. Later papers [5]-[7] further investigated the possibilities of the IFEL as an "advanced accelerator" technology and incorporated advances in FEL theory in their analysis. Until now[8,9], however no experiment has been performed which tests any of these suggestions.

In recent years the search for advanced accelerator technology has intensified due to the limitations of conventional klystron linac technology[10]. In response to this many accelerator schemes have

been proposed (i.e. Plasma Beat Wave Accelerator, Laser Wakefield Accelerator, Laser Beat Wave Accelerator[11]-[14]) using short wavelength radiation either independent of or in conjunction with a plasma.

For these reasons, the absence of experimental verification of the IFEL concept and the growing need for new reliable accelerator designs, we have configured and performed an IFEL experiment to explore the FEL physics of such a device. Our experiment involves the acceleration of electrons to energies of order 1MeV from an initial energy of 750 keV. At present these energies are readily obtained using other existing technologies. Our project is therefore a "proof of principle" experiment intended to verify the theoretical predictions of FEL physics as they relate to the IFEL.

1.2 THE FEL

In an FEL a "cold" electron beam enters a device known as an undulator. The undulator provides a periodic magnetic field, period λ_w, induced by a series of magnets with opposite polarities (see figure 1).

FIG. 1

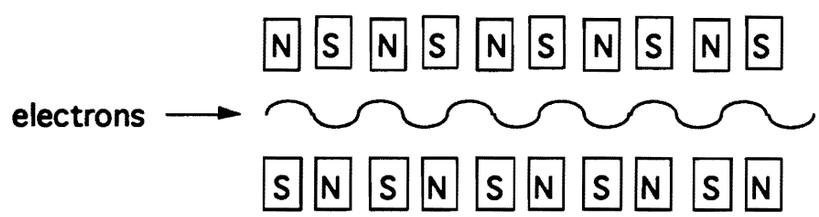

Figure 1 shows an linear undulator comprised of individual permanent magnets. An alternative undulator configuration, and the one used in our experiment, is the bifilar helical undulator which is built by winding two wire helices carrying opposing currents. This creates a helical periodic transverse magnetostatic field on the axis of the windings. The magnetic field causes a transverse periodic motion of the electrons as they pass through the undulator and this causes a constructive interaction to develop between the electron motion and a travelling wave electromagnetic signal. The relation between the period of the magnetic field in the undulator and the wavelength of the amplified electromagnetic signal is[15]:

$$\lambda s = [\lambda_w/2\gamma^2](1+a_w{}^2) \tag{1.1}$$

where λ_s is the wavelength of the signal, λ_w is the undulator period and a_w is the "wiggler parameter" which is a measure of the ratio of the transverse to parallel velocity of the electrons (i.e. $a_w=\gamma(v_x/v_z)$) and is proportional to the strength of the transverse magnetic field, $B_\perp$, in the undulator. When λ_w and γ satisfy this relationship, as the electron moves down the one undulator period, the optical signal move ahead of the electron by one optical period thus the electron and the optical wave remain in a fixed phase relationship as they move down the undulator.

In the following treatment we discuss the elementary physics of an FEL which operates in the "Raman" regime[16,17]. In the Raman regime collective effects present in the electron beam must be included in the analysis; these effects become important when the

electron density of the beam is large (i.e. $\omega_p L/\gamma c >> 1$ where L is the length of the interaction and $\omega_p=\sqrt{4\pi n_o e^2/\gamma m}$ is the invariant plasma frequency where n_o is the electron density in the laboratory frame and m is the electron rest mass). In addition the strength of the magnetic field in the undulator must not be too large[15] (i.e. $eB_\perp/mc << \sqrt{2k_w\omega_p L/\beta\gamma^2}$) for the Raman regime analysis to be appropriate. This is the situation in our experiment, but not necessarily in other experiments involving high energies and strong undulator fields. We begin by considering the dispersion relation for a cold electron gas in the rest frame of the relativistic electrons.

The dispersion relation is:

(1.2) $$\omega' = \pm\ \omega_p$$

Where ω' is the electrostatic solution to the dispersion relation and ω_p is the frequency of the electrostatic or space charge wave in the electron rest frame. By applying a relativistic Lorentz transformation in the laboratory frame we find:

(1.3) $$\omega = \mathbf{k}\cdot\mathbf{v} \pm\ \omega_p/\gamma$$

Where **v** is the velocity of the electrons and **k** is the wavenumber of a periodic disturbance on the electron beam when viewed in the laboratory frame. Notice that the dispersion relation reveals two modes for the electrostatic wave in the laboratory frame. If we now include a nonzero transverse magnetic field $B_\perp$ from the undulator, another periodicity $k_w\cdot v=k_w v_{||}$ results, and the dispersion relation is:

(1.4) $$\omega = (k+k_w)v_{||} \pm \omega_p/\gamma$$

where k_w is the undulator wavenumber. The phase velocity for these modes is:

(1.5) $$v_p = \frac{\omega}{k} = v_{||} \frac{\omega}{\omega \pm \omega_p/\gamma}$$

We see that each mode yields a different phase velocity. We refer to these two modes of the phase velocities as the fast and the slow electrostatic wave or the fast and slow space charge wave. The phase velocity of the fast space charge wave is greater than the beam velocity $v_{||}$ and that of the slow space charge wave is less than $v_{||}$.

Figure 2 is a plot of the dispersion relation for the two space charge modes superimposed on the light line of an EM wave propagating through a waveguide. In an FEL the interaction point of the slow space charge wave and the light line is approximately at the wavelength satisfying the FEL relation mentioned above in eq. (1.1): The equation for the point of interaction which involves the dispersion relation of the waveguide is:

(1.6) $$\omega_s = c[k_\perp^2 + k_s^2]^{1/2} = (k_s+k_w)v_{||} \pm \omega_p/\gamma$$

Where $k_\perp$ is the transverse eigenmode of the waveguide being excited. In the equation for the optical frequency we find the term ω_p/γ; this term introduces a "Raman shift" in the resonant frequency of the FEL. The Raman term introduces a correction to equation 1.1

and must be included when the FEL operates in the Raman regime (i.e. $\omega_p L/c >> 1$ and $\Omega_\perp << \sqrt{2k_w\omega_p L/\beta\gamma^2}$).

FIG. 2

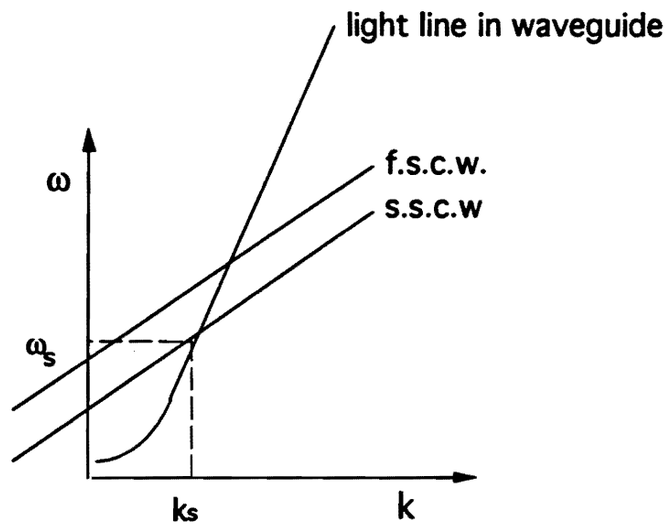

The intersection of the electrostatic and electromagnetic dispersion plots occurs for both the fast and the slow space charge waves. The fast space charge wave presents a stable perturbation to the beam since the electrons must gain energy in order to excite it. The slow space charge wave however can be excited by electrons which lose energy to this mode of the electrostatic wave and thus it is an unstable perturbation to the beam which will grow and cause the bunching of the electrons as the beam propagates. The lost kinetic energy of the electrons is transferred mostly to the growing radiation field thus causing the amplification of the electromagnetic signal (which in our case starts from cathode shot noise) as it propagates down the undulator. This process is referred to as

"stimulated emission". Some energy, though much less, is transferred to the electrostatic slow space charge wave "bunches" themselves.

1.3 THE IFEL

The IFEL is a device which relies on the same physical principles as the FEL with the difference being that in this case the desired result of the interaction in the undulator is the acceleration of the injected electrons. In the IFEL a coherent high intensity radiation field (i.e. a laser beam) propagates colinearly with the injected electron beam along the undulator. If the parameters of the undulator are chosen correctly the dispersion equation of the EM wave can be made to intersect that of the fast space charge wave on the dispersion plot in figure 2; the two waves then strongly interact at a common frequency and wavenumber. The fast space charge wave will grow at the expense of the radiation field of the signal. The growth of the fast space charge wave and the resulting electron acceleration at the expense of the signal power results from stimulated absorption. In order to maintain the IFEL resonance condition for the length of the undulator either the spatial period or the magnetic field strength in the undulator is reversed tapered (i.e. $\frac{d\lambda_w}{dz}>0$) to accommodate for the change in energy (i.e. the γ value) as the electrons are accelerated. This reverse tapering of the undulator in the case of the IFEL is analogous to the undulator period tapering in a conventional FEL[18] which is used to enhance the efficiency of the FEL and has been demonstrated to do so[19].

1.4 THE IFELA

The experiment which we have performed and which will be described at length in this thesis involves the "Inverse Free Electron Laser Auto-Accelerator" [IFELA]. The IFELA is a hybrid device which functions both to regenerate radiation as a conventional FEL oscillator as well as to accelerate electrons as an IFEL. Figure 3 is a schematic diagram of the IFELA.

FIG. 3

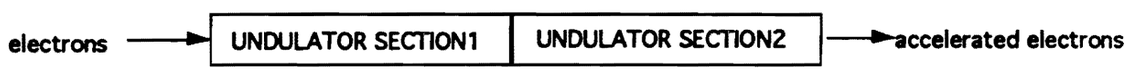

The first undulator section in the IFELA has a constant period magnetic field $B_\perp$ and performs like a conventional FEL oscillator. The undulator here is designed to generate high power at wavelengths which satisfy the FEL resonance relation. The high power produced from the FEL interaction in the first section will propagate into the second section of the undulator. The spatial period in the second section is larger than that of the first section and is designed to absorb the radiation generated there. This absorbed radiation supplies the energy necessary to accelerate a certain group of the electrons which enter the second section. The spatial period in the second section is reverse tapered to maximize the acceleration efficiency in that section. In this way, for a certain group of electrons,

as their γ increases the undulator period λ_w increases so as to maintain the resonance relation (eq. 1.1).

The absorption which occurs in the second section can be considered as an additional loss mechanism of the entire oscillator cavity. The IFELA is designed such that the oscillation threshold condition is satisfied (i.e. gain per pass > loss per pass) allowing the intracavity signal power to reach the saturation[20] level.

Figure 4 is a superposition of the dispersion diagrams for both sections of the undulator and the light line. In the first undulator section the intersection occuring between the light line and the slow space charge wave (s.s.c.w.1) results in the amplification of the electromagnetic signal characterized by ω_s and k_s. In the second section the same point of intersection (i.e. the same ω_s and k_s) occurs between the fast space charge wave (f.s.c.w.2) and the lightline. This mode of the electrostatic wave is now excited by the electromagnetic signal generated in the first section because the undulator period has been increased in the second undulator section thus translating the electrostatic dispersion relation down the figure. The interaction of the two waves results in the acceleration of some of the electrons.

FIG. 4

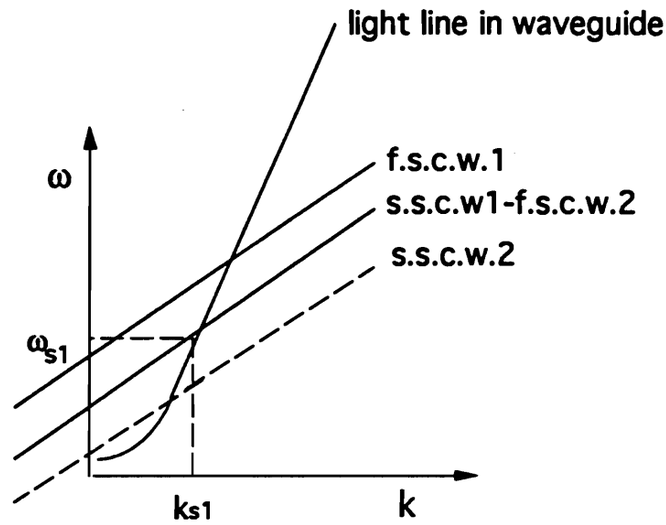

The need to generate the high intensity (~ MW's/cm^2) EM signal within the resonator itself is due to the absence of any conventional source of high power coherent radiation near the design wavelength of ~1.65 mm which can be produced by our apparatus. One drawback involved in this less than ideal experimental configuration(i.e. signal amplification and absorption occur within the same device) is that the electron beam entering the second section has a broadened energy distribution as a result of the FEL interaction taking place in the first section. This broad energy distribution can have deleterious effects on the IFEL interaction taking place in the second section as we will see in Chapter 2. The phase space of the electrons is "smeared" out due to the FEL interaction in the first section and only a small window of the phase space electrons can participate in the IFEL interaction in the second undulator section. Another drawback

involved with this configuration is that the amount of power in the accelerated beamlet cannot exceed the amount of power generated by the device. In the standard IFEL accelerator the power is supplied externally by a conventional laser. The externally supplied laser radiation is not limited, thus the amount of power absorbed can be arbitrarily large.

In this thesis we will discuss the properties of the IFELA and its ability to absorb radiation as well as accelerate electrons. In Chapter 2 we discuss the theoretical basis of the FEL as well as the IFEL mechanism. Chapters 3 and 4 will describe the experimental arrangement of the IFELA experiment that we have performed. In Chapters 5 and 6 we discuss and present the data collected in the experiment. In Chapter 7 we will discuss the possibility of using an external laser to supply the high intensity coherent radiation that is requisite for the IFEL interaction to take place, in addition we will discuss cases involving a high energy (50MeV) injected beam where the electrons are accelerated to energies that are of technical interest.

Chapter 2

IFEL THEORY

2.1 INTRODUCTION

In this chapter we present the equations used to describe the electron dynamics and the evolution of the electromagnetic wave in an FEL. We will show what conditions must be imposed on these equations in order to insure particle acceleration. The equations presented here were first derived for the low current density case in a paper by Kroll, Morton and Rosenbluth[21] and modified by S.Y. Cai[22] for the case of finite space charge, as is the case in our experiment. They are derived from classical Electromagnetic theory and do not include quantum mechanical effects. Quantum effects become significant when the initial particle momentum and photon momentum are of comparable magnitude[23] (i.e. $hk \approx p_0$), a condition far from satisfied in our experiment. The classical equations are incorporated into the numerical simulations used to design our experiment as well as to explore the sensitivity of the IFEL's performance to changes in various parameters. Later in the chapter we present the numerical results for the resultant energy spectrum and signal wave evolution as they relate to changes in initial power level and undulator field strength in the FEL. Finally, we develop an analytical expression, based on the FEL equations, for the optimal tapering parameter to be used in an IFEL. In the following discussion we ignore losses due to synchrotron

radiation[24} which become significant for values of $\gamma \leq (3a_s k_s/2a_w k_w 2r_e)^{1/3} \cong 7500$ *; for a complete study of the effect of synchrotron radiation losses in an IFEL see ref[5].

* Where we use the values of a_w, k_w, a_s, k_s from our experiment and where $r_e = e^2/mc^2$ is the electron radius.

2.2 FEL EQUATIONS

In the FEL a relativistic electron beam enters an undulator. The undulator induces a periodic transverse motion of the electron beam which is in the same plane as the electric field of the EM wave. The transverse motion of the electron beam which is parallel to the electric field of the signal wave allows for the exchange of energy between the two through the $J_\perp \cdot E_\perp$ term of the electromagnetic energy equation. The oscillating magnetic field of the signal wave is of primary importance in that its cross product with the electron transverse velocity $-e/c(v_\perp \times B_s)$ produces an axial force called the "Pondermotive Force". This force causes an axial bunching of the electron beam such that the net result of the interaction of the electron bunches with the EM signal is to amplify the radiation to high power levels. We define a phase angle ψ which describes the phase between these electron bunches and the wavefronts of the EM wave:

$$\psi = (k_w + k_s)z - \omega t + \Phi$$

where k_w and k_s are the wavenumbers of the undulator and signal wave respectively, ω is the signal frequency and Φ is the optical

phase which varies as a function of position as the wave propagates down the axis. Taking the derivative of ψ with respect to position along the axis we find:

$$(2.1)\quad \frac{d\psi}{dz} = k_w + k_s - \frac{\omega}{v_z} + \frac{\partial\Phi}{\partial z}$$

where v_z represents the parallel beam velocity. Using the relation** $P_\perp = \frac{e}{c}A$ where $P_\perp$ is the initial transverse momentum of the electrons and A is the total magnetic vector potential (i.e. $\nabla \times A = B_{undulator} + B_{signal}$) we can show:

(** This condition is satisfied for the case of the FEL since the initial transverse beam momentum is small ≈ 0)

$$(2.2)\quad \frac{v_z}{c} = \sqrt{1 - \frac{1 + a_w^2 + 2a_w\, a_s \cos\psi_i}{\gamma_i^2}}$$

Where $a_w = eB_\perp/k_w mc^2$ is the normalized vector potential of the undulator and $a_s = eE_o/k_s mc^2$ is the normalized vector potential of the signal wave and where the subscript i denotes the ith particle. We can rewrite eq.(2.1)

as:

$$(2.3)\quad \frac{d\psi_i}{dz} = k_w + k_s - \frac{k_s}{\sqrt{1 - \frac{1 + a_w^2 + 2a_w\, a_s \cos\psi_i}{\gamma_i^2}}} + \frac{\partial\Phi}{\partial z}$$

The energy of the particles in the undulator is described by the equation:

$$(2.4)\quad \frac{d\gamma_i}{dz} = -\frac{a_w a_s k_s}{\gamma_i} \sin\psi_i + \frac{2\omega_p^2}{k_s c^2} [\langle\cos\psi\rangle \sin\psi_i - \langle\sin\psi\rangle \cos\psi_i]$$

where $\omega_p^2=4\pi n_o e^2/\gamma m$ is the invariant plasma frequency and is directly proportional to the electron density in the beam and where <--> indicates the ensemble average value for all the electrons.

Finally the two dimensional wave equation for the signal wave is:

$$(2.5)\quad (\nabla_\perp^2 + 2ik_s\frac{\partial}{\partial z} + 2i\frac{\omega}{c^2}\frac{\partial}{\partial t})\, u(r,t) = -F\frac{\omega_p^2 a_w}{c^2} < \frac{e^{-i(\psi-\Phi)}}{\gamma} >$$

where $u(r,t)= a_s(r,t)e^{i\phi(r,t)}$ is the complex field amplitude of the signal and where $\nabla_\perp^2$, the transverse Laplacian, involves Bessel functions to simulate waveguide effects. In the equation we assume that the complex wave amplitude slow varying hence only the first time and axial space (i.e. z) derivative are included. Also included is the effect caused due to the electron beam radius being smaller than the waveguide radius (i.e. the "Filling Factor" F). It is instructive to note that the driving term for the wave equation is related to the product of the electron density ($n_o \alpha \omega_p^2$) and the vector potential of the undulator field (a_w).

We can alternatively derive equations 2.3 and 2.4 using a Hamiltonian formalism[25], describing the interaction of single electron with the signal in the presence of an undulator, developed by Kroll, Morton and Rosenbluth:

$$(2.6)\quad H(\Delta\gamma,\psi) = \frac{k_w(\Delta\gamma)^2}{\gamma_r} + F(\psi)$$

where $\Delta\gamma= \gamma - \gamma_r$ and γ_r is the resonant energy. The function F:

$$(2.7)\quad F(\psi) = -k_s a_s a_w(\cos\psi + \psi\sin\psi_r)/\gamma_r$$

is called the ponderomotive potential. In looking at the behavior of the ponderomotive potential function we find that potential wells are formed along the undulator which define the electron bunches. The position of these wells or "ponderomotive buckets" depends on the value of the resonant energy γ_r. By changing a_w as a function of position we can change the resonant γ_r. This prevents electrons from falling out of phase with the signal as their energy falls or rises, and allows them to continue participating in the interaction therby enhancing the signal gain or electron acceleration as the case may be. Figure 1 shows the ponderomotive potential for a typical reverse tapered IFEL.

FIG. 1

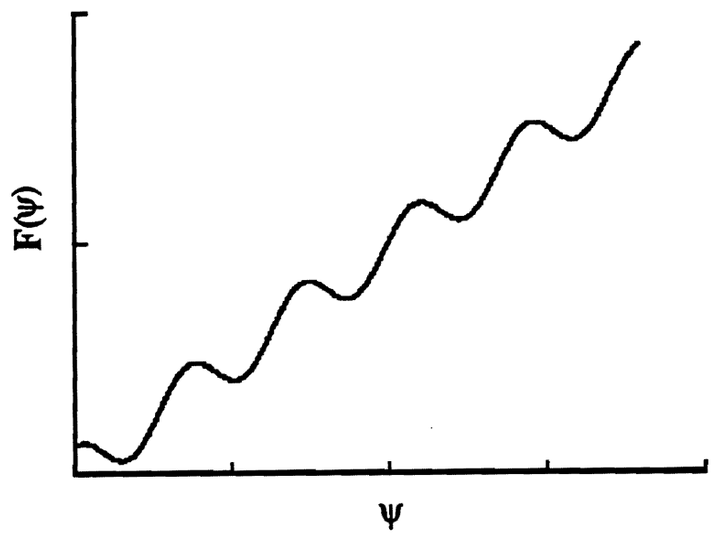

Notice that the center of the bucket rises along the undulator thus maintaining the resonance as the electrons gain energy.

2.3 CONDITIONS IMPOSED ON FEL EQUATIONS TO INSURE ACCELERATION

In viewing eq.(2.4) we can see that for the case of acceleration ψ must be such that $\frac{d\gamma}{dz} > 0$. To maintain this acceleration resonance we require ψ, the phase angle, to be constant thus we set eq.(2.3) to zero (i.e. $\frac{d\psi}{dz}=0$). This results in the relation:

$$(2.8)\quad k_w \approx k_s\left(\frac{1+a_w^2+a_w a_s \cos\psi}{2\gamma_i^2}\right)+\frac{\partial\Phi}{\partial z}$$

using eq.(2.8) in eq.(2.4) and neglecting the optical phase change and terms proportional to $a_s \ll a_w$ we obtain:

$$(2.9)\quad \frac{d\gamma_i}{dz} = -\frac{a_s k_s}{\gamma}\sqrt{1+\frac{2\gamma_i^2 k_w}{k_s}}\,\sin\psi_i + \frac{2\omega_p^2}{k_s c^2}\left[\langle\cos\psi\rangle\sin\psi_i - \langle\sin\psi\rangle\cos\psi_i\right]$$

If we vary the undulator period $\lambda_w(z)$ in our accelerator section leaving all other parameters unchanged we find:

$$\frac{d\gamma_i}{dz} = -\,a_s k_s\sqrt{\frac{1}{\gamma_i^2}+\frac{2\lambda_s}{\lambda_w(z)}}\,\sin\psi_i + \frac{2\omega_p^2}{k_s c^2}\left[\langle\cos\psi\rangle\sin\psi_i - \langle\sin\psi\rangle\cos\psi_i\right]$$

By varying only the magnetic field strength $B_\perp$ in the undulator we find:

$$\frac{d\gamma_i}{dz} = -\,a_s k_s\sqrt{\frac{\Omega(z)}{\omega\gamma_i}}\,\sin\psi_i + \frac{2\omega_p^2}{k_s c^2}\left[\langle\cos\psi\rangle\sin\psi_i - \langle\sin\psi\rangle\cos\psi_i\right]$$

Where $\Omega(z) = eB_\perp/mc$ is the Larmor frequency. Finally if we vary the undulator parameter $a_w(z)$ which involves the product of the period and the magnetic field we find:

$$\frac{d\gamma_i}{dz} = -\frac{a_w(z)a_s k_s}{\gamma_i}\sin\psi_i + \frac{2\omega_p^2}{k_s c^2}[\langle\cos\psi\rangle\sin\psi_i - \langle\sin\psi\rangle\cos\psi_i]$$

In all these cases we find that $\frac{d\gamma}{dz}$ is sensitive to changes in the system parameters and that the proper choice of taper is crucial for obtaining the desired acceleration gradient.

2.4 NUMERICAL SIMULATION RESULTS

In this section we will explore the IFELA's performance as a result of changes in various system parameters used in the numerical simulation. The simulation code, developed by S.Y. Cai[22], uses the two dynamical equations for 1D electron motion as well as the 2D wave equation presented in section 2.2. In the code a group of test electrons (~ 5000) is initially set in a cylindrical grid having the radial dimension of the electron beam. The electrons are each assigned an initial phase angle ψ_i distributed equally, from 0-2π, over the phase angle ψ. They are injected mono- energetically into the undulator and the three aforementioned equations are then solved self consistently, using the Adams-Bashford[26] numerical method for solving partial differential equations, as the electrons traverse the undulator. The bessel functions used in the wave equation correspond to a TE_{11} mode for the signal in the waveguide.

The code is a single pass code and starts with a small initial signal. Table I shows the parameters used in the simulation chosen to closely match those used in the experiment.

TABLE 1

Injection Energy	800kV
Beam Diameter	4mm
Beam current	150A
Pulse length	150nsec
Drift tube diameter	11mm
<u>Undulator: first section</u>	
period	1.43cm
$B_\perp$	620G *(a_w=0.083)
length	37.5cm
<u>Undulator: second section</u>	
period	1.8-2.25cm
taper	$\frac{d\lambda_w}{dz}=0.0116$
$B_\perp$	400G *(a_w=0.053)
length	36.5cm
$a_s(z=0)$	7×10^{-4} (Initial intensity on axis ~.3 MW/cm2)
λs	1.65mm

* This value does not include the effect of the guide field on a_w (i.e. the Magnetoresonance term) see chapter 3 section 4 for a discussion of this effect.

Figure 2 shows the electron energy spectrum, which enters the undulator as a cold beam (i.e. $(\delta\gamma/\gamma)_{||} \approx 0$), after it has passed through

the first section of the undulator. In the figure we see the characteristic broadening of the electron energy spectrum after the FEL interaction. Also note the downshift in the average electron energy ($\Delta\gamma$) resulting from the FEL interaction in the first section. The efficiency η of the FEL is directly related to the downshift $\Delta\gamma$ of the mean electron energy by the relation $\eta=\Delta\gamma/(\gamma-1)$. This energy broadened beam enters the second section of the undulator where the acceleration occurs.

FIG. 2

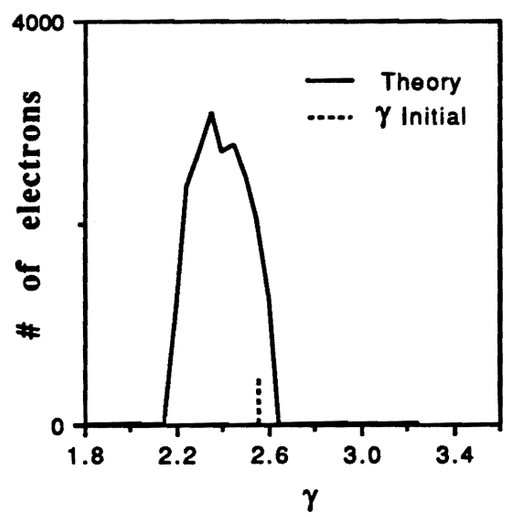

Figure 3 shows the energy spectrum for particles exiting the second section of the undulator. In the figure we see that a small subgroup of particles is accelerated to $\gamma \sim 3$ corresponding to an energy gain of ~ 250keV.

FIG. 3

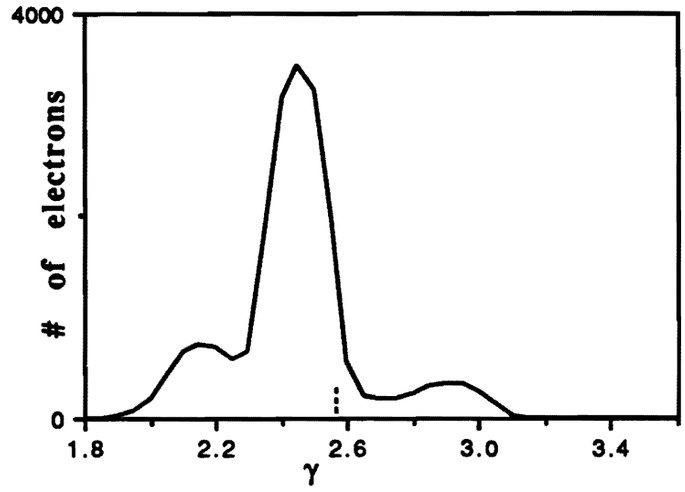

Close inspection of the accelerated particles shows that they represent ~9% of the total population. We can see from the figure that the main body of the particles remain downshifted in energy. A small concentration of electrons exists at γ ~2.1; this feature was further investigated and found to occur independent of the acceleration process.

The electron energy spectrum resulting from the case involving a constant period in the second section of the undulator is quite different from the above result. Figure 4 is a plot of the resultant electron energy spectrum when the undulator period in the second section is kept at a constant value; notice that in the figure we do not see any "bump" at the high energy end of the spectrum, rather we see a sloping "shoulder" that decreases monotonically with increasing energy. The cause for this significant difference is that in the constant period case those electrons initially satisfying the resonance

condition quickly fall out of resonance after the initial acceleration interaction, other electrons which subsequently satisfy this constant resonance condition (these electrons are far off resonance in the tapered case) are then accelerated. Thus in the spectrum we see a large number of electrons that are accelerated to energies slightly above the injection energy with the number of electrons decreasing as the energy gets larger.

FIG. 4

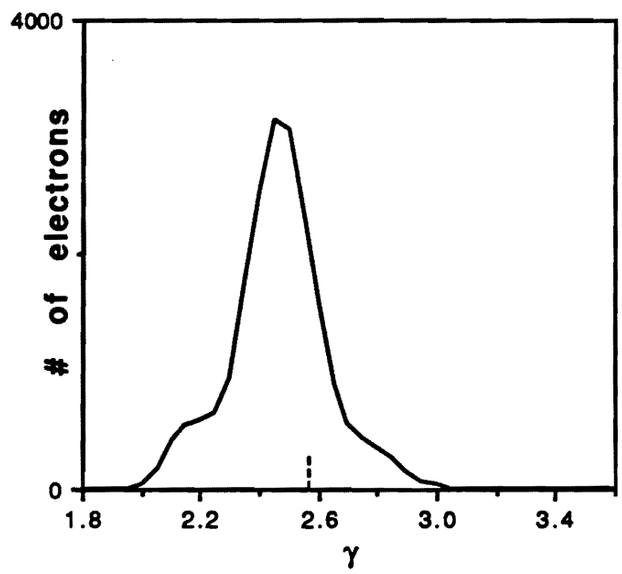

Figure 5 represents the evolution of the signal wave on the beam axis. In the figure, we note the characteristic exponential power gain in the first section which terminates at z=37.5cm, followed by a precipitous drop in the second section that is caused by stimulated absorption. The numerical result for the signal gain in the first section is ~ 7 indicating a power gain ~ 50. This is consistent with the observed gain for an undulator similar to our own operating in the

Columbia FEL[27]. The initial value of the wave amplitude is chosen in accordance with the calculated power at the beginning of a single pass through the resonator cavity after the onset of sustained oscillation.

FIG.5

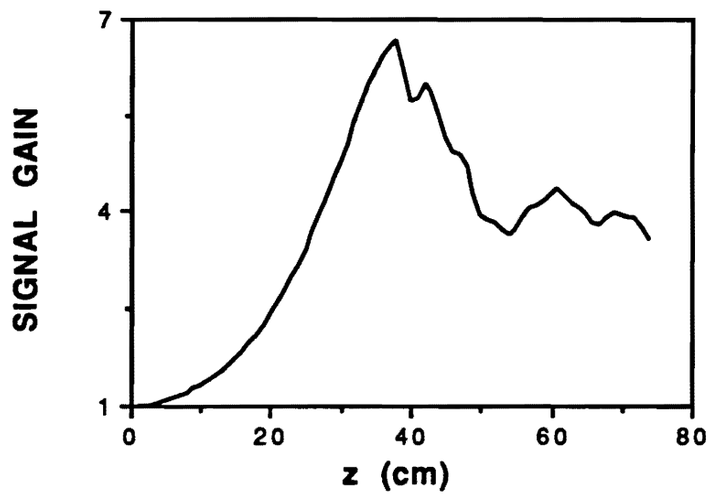

In the experiment losses result from the cavity mirrors which each have a reflectivity of >85%, attenuation by the waveguide ~ 50%, signal absorption ~40%, and coupling losses due to mode distribution ~ 75%. The combination of these loss mechanisms results in a power drop of ~ 1/30 as the signal begins the next pass. Thus the design parameters (i.e. undulator lengths, magnetic field strengths, and initial power level) used in the simulation and realized in the experiment are such that an overall power gain >30 is achieved in the oscillator cavity so that oscillation can be sustained. In the second half of the figure the signal amplitude drops by a factor of ~ 50%

corresponding to a power drop of ~ 75%. It should be noted here that in the numerical simulation only radiation at the carrier wavelength is considered, however roughly 1/3 of the power generated in the FEL is in the form of sideband radiation[28], which was found to be unaffected (i.e. not absorbed) during the acceleration process[9].

It is instructive to view the evolution of the electrons in phase space as they traverse the entire undulator. Figure 6 a-e , is a phase space diagram obtained from the simulation; 6a is the phase space at z=15cm, 6b for z=30cm, 6c for z=45cm, 6d for z=60cm and 6e for z=74cm the end of the undulator. In 6a we find that as the electrons become trapped in the ponderomotive buckets those particles with $\sin\psi < 0$ are upshifted in energy and those with $\sin\psi > 0$ are downshifted. In 6b the fraction of electrons downshifted in energy is clearly greater than those upshifted. This downshift corresponds to the mean electron energy loss that takes place in the first section of the undulator, which functions as a standard FEL, resulting from the stimulated emission of radiation. In 6c we see the phase space of the electrons after they have entered the second section of the undulator; notice that a small group of electrons can be found at energies higher (~150-200keV) than the injection energy $\gamma \sim 2.5$. Some particles with the proper phase are nonetheless not accelerated due to the fact that they have "fallen" out of the potential buckets. We also find in 6c that a large number of particles have now been downshifted to lower energies $\gamma \sim 2.15$; this concentration of particle corresponds to the low energy bump in fig. 3. In 6d we begin to see the characteristics of the final energy spectrum, a large concentration

FIG. 6

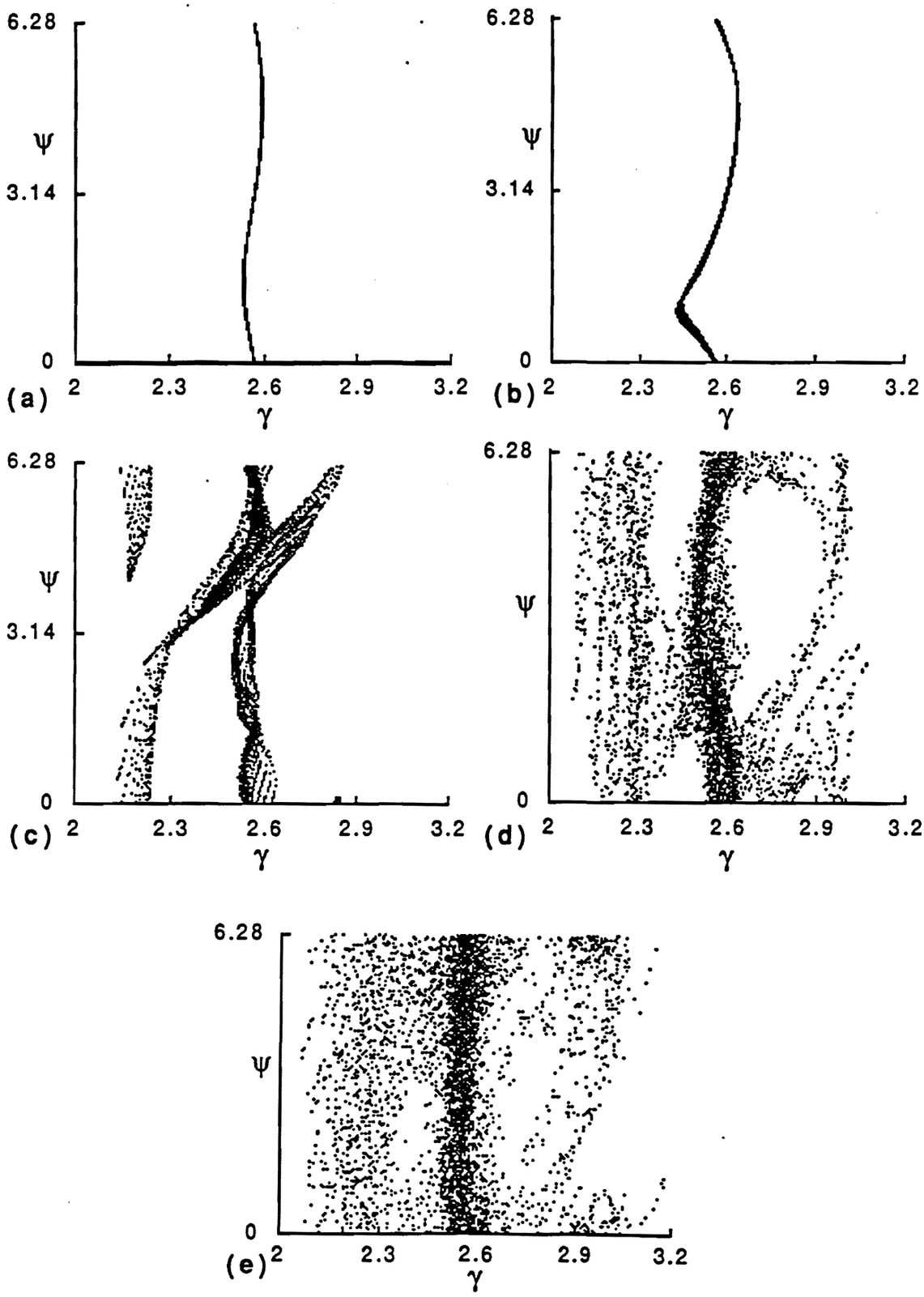

of electrons is located very near the initial energy while a group of electrons can be found at values as high as $\gamma = 3$. The electrons located at low energies are more evenly distributed along ψ at this later stage. Finally 6e, which is the phase space at the end of the second section, shows that some electrons are accelerated up to energies with γ=3.2 while the main body of the electron population is close to the initial energy and a large number are at smaller energies.

The numerical simulation studies performed, and presented in what follows, were viewed as an aid in the design of the experiment and the interpretation of the results. Some parameters such as the tapering parameter and the undulator length were not varied in the simulation because they were built into the experimental apparatus. The field strength in the undulator is a controlled parameter and the power level varies widely from shot to shot, thus we have done numerical studies to determine how the IFELA's performance is affected by variations in these parameters.

If the initial power level is increased by one order of magnitude (Fig.7) we find that an increased number of particles is accelerated. However, the maximum energy attained by the accelerated particles remains the same. This follows from the resonance relation in Chapter 1 $\lambda s=\lambda_w/2\gamma^2$ which yields $\Delta\gamma/\Delta z \propto \Delta\lambda_w(z)/\Delta z$. Thus the acceleration gradient is limited by the tapering parameter $\frac{d\lambda_w(z)}{dz}$. It is found that at a high initial power level $a_s=4.25\times10^{-2}$ (Intensity≈2

GW/cm^2 on axis) as much as 65% of the electrons can be accelerated in the IFELA.

FIG. 7

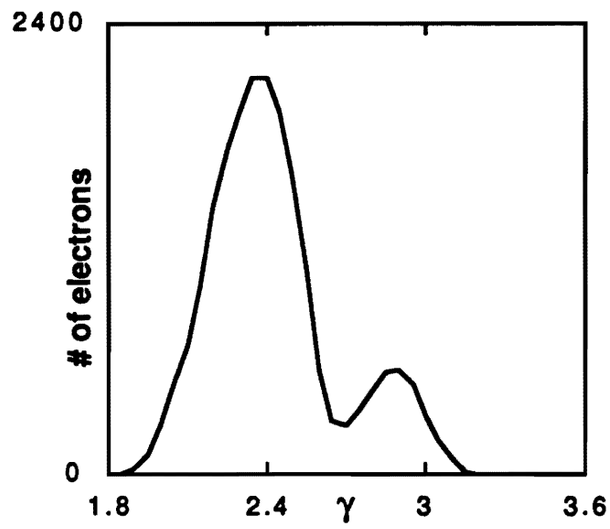

By varying the wiggler parameter a_w in the second section the performance of the IFELA is changed significantly. Figure 8 shows the resultant electron energy spectrum from the simulation for the case where the magnetic field strength $B_\perp$ in the undulator second section is reduced to $B_\perp$=250G. In the figure we find that fewer particles are accelerated with the lower field value. The reason for fewer accelerated particles stems from the diminished "bucket height" (i.e. $\Delta\gamma/\gamma \propto \sqrt{a_s a_w}$) for this case since $a_w \alpha B_\perp$. The bucket height represents the height of the ponderomotive potential well and is roughly proportional to the fraction of electrons that can participate in the acceleration process. The maximum energy to which particles are accelerated remains the same as the case using

the higher undulator field. This follows from the result derived previously for the case of high input power, namely the parameter determining the acceleration gradient for the IFELA is $\frac{d\lambda_w(z)}{dz}$.

FIG. 8

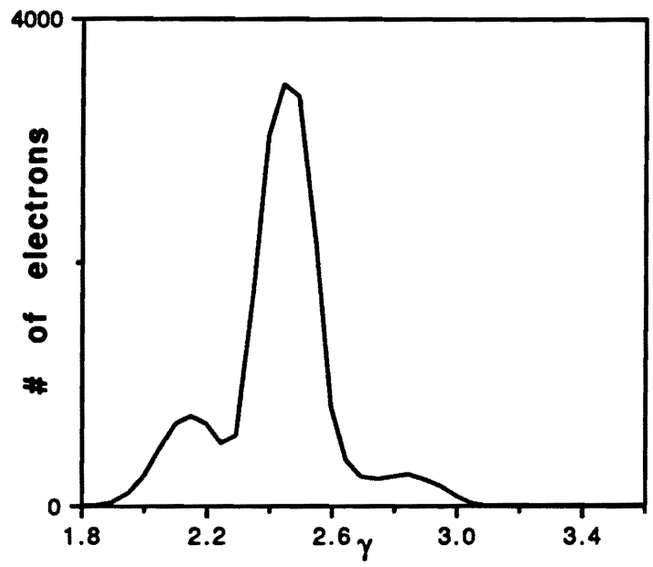

If we raise the undulator field in the second section (i.e. $B_\perp$ = 1000G) virtually no acceleration takes place as can be seen from figure 9. This result can be traced to the behavior of the ponderomotive potential as it changes along the z axis. In sect 2.1 we saw that for the ponderomotive potential:

$F(\psi) = -k_s a_s\, a_w(\cos\psi + \psi\sin\psi_r)/\gamma_r$,

the character of F is determined by the linear component of the function as well as the oscillatory part as can be seen graphically in

fig. 1. The linear component is directly proportional to ψ. At higher values of a_w, we find from eq.(2.3) that, ψ grows more rapidly along the axis. The effective height of the ponderomotive buckets is not only proportional to the coefficient $-k_s a_s a_w$ it is also affected by the asymmetry (resulting from the $\psi \sin\psi_r$ term) of the "bucket walls"; when the linear component of the potential becomes too great the effective bucket height becomes severely diminished and virtually no electrons participate in the acceleration process.

FIG. 9

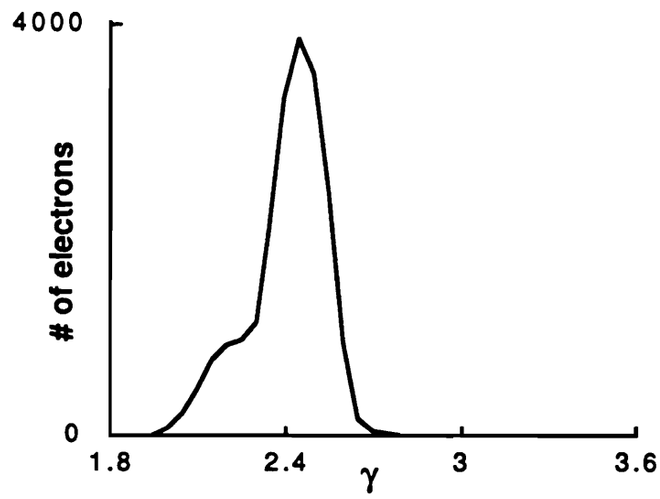

Use of this high value for the transverse magnetic field in the experiment led to the breakup of the electron beam as it enetered the second section and thus no experimental results were found for this case.

2.5 STIMULATED EMISSION/ABSORPTION IN THE UNDULATOR

In order to examine the ability of the IFELA to absorb radiation a further investigation of the FEL gain spectrum is necessary. According to FEL theory[15] the gain spectrum of an FEL is sensitive to changes in the energy of the relativistic electron beam, the brightness of the beam and the initial power level of the radiation. In this section we will first see the gain spectrum for the IFELA as a function of γ where the power growth in the simulation closely resembles the experimental values. The value we use for the initial power level is ~ 0.3MW/cm^2 on the axis. This value corresponds to the power present at the beginning of one pass in the oscillation cavity after allowance is made for the cavity losses (see the previous section for a discussion of the cavity losses).

Figure 10 is a numerically generated plot of the gain spectrum for only the first section of the undulator (length=37.5 cm) which acts as a conventional FEL. We can see from the figure that depending on γ the undulator can amplify as well as absorb radiation. The shift from gain to loss in the plot is a result of the change in the phase angle ψ which causes a sign change in $\frac{d\gamma}{dz}$ (from equation 2.4) and shifts the direction of the energy exchange between the signal and the electron beam.

FIG. 10

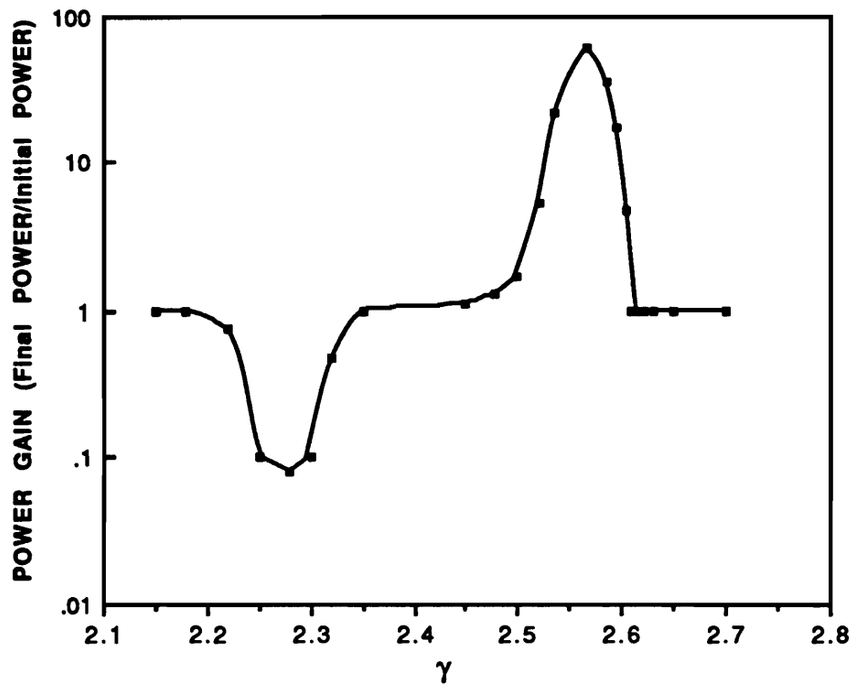

In figure 11 we find that if the radiation generated in the first section of the undulator is allowed to propagate further along with the electron beam into a second section with a different period (i.e. such that λ_{w2} causes $\frac{d\gamma}{dz}$ to change sign) the power is absorbed in that section. In the figure both the case λ_{w2}=const. as well as $\lambda_{w2}=\lambda_{w2}(z)$ is shown (the exact values used for λ_{w2} = const. and the function $\lambda_{w2}=\lambda_{w2}(z)$ were presented in the previous section).

FIG. 11

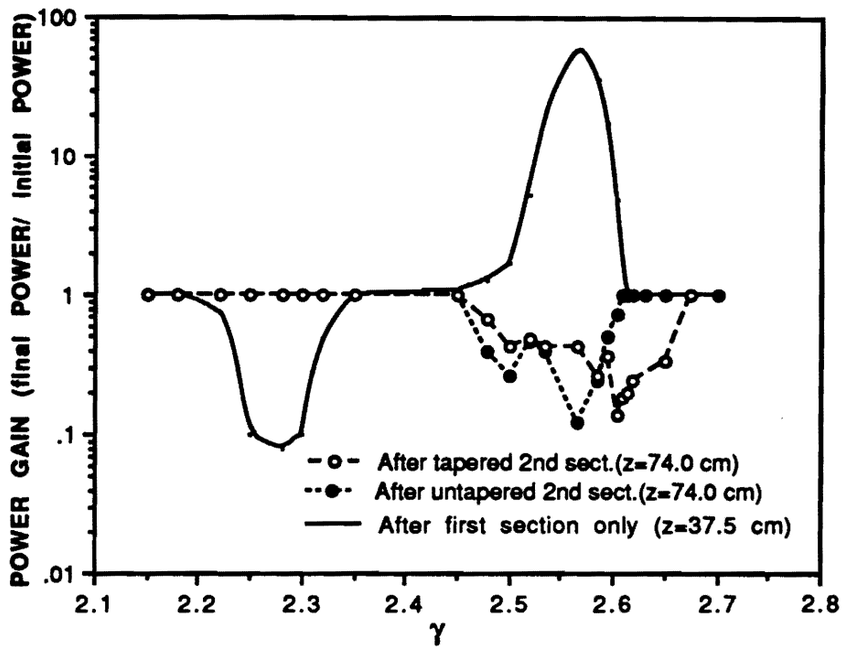

(Note: In the figure, the gain spectrum after the first section corresponds to a cold beam(i.e. $\delta\gamma/\gamma$ ~0) with initial signal power ~0.3 MW/cm^2 on axis. However, the beam entering the second section is energy-broadened and bunched as a result of the FEL interaction which takes place in the first section and the signal power entering the second section is ~15MW/cm^2 on axis)

The non-linear absorption spectra for the two cases are comparable in the amount of absorption achieved for each case. The resonant energy for maximum absorption is shifted to a slightly higher energy in the tapered case which is not surprising since the resonant energy increases as λ_{w2} gets larger in the tapered case. Despite the comparable absorption values for the two examples, the energy distribution of the exiting electrons is

quite different. In Section 2 Eq. 2.7 we saw that only those electrons whose phase space values fall within the pondero- motive potential wells (i.e. "buckets) can interact with the electromagnetic signal. In the untapered case the center of the buckets remains at a constant value, hence, those electrons which are initially accelerated due to the interaction quickly fall out of the bucket as their energy increases. In the tapered case, however the center of the bucket rises as the electrons gain energy thus allowing the electrons to continue participating in the acceleration process. We saw in the last section that the resulting energy spectra for each of these cases are quite different (see figures 3 and 5).

Finally in figure 12 we see the effect of a "hot beam" on the amplification and absorption properties of the IFELA. The ability of the first undulator section (which acts as a conventional FEL) to amplify radiation is significantly reduced as the energy spread of the electron beam grows. This effect is due to the fact that for net gain in the FEL we require that the electrons be "trapped" in the ponderomotive buckets at a high γ value and drop down down in the potential well yielding their lost energy to the electric field of the radiation. If the value of the energy spread in the beam is greater than the height of the potential well[7] (i.e. $\Delta\gamma/\gamma \sim \sqrt{a_w a_s}$) no net drop in beam energy and hence no amplification of the radiation takes place. Similarly in the absorption process, if the energy spread of those electrons trapped in the potential well exceeds the bucket height in the second section. Then the net absorption in that section is minimal since roughly equal numbers of electrons lose or gain energy during the interaction. If the energy spread of the beam is

somewhat less than the bucket height in a given undulator section then those electrons possessing energies at the bottom of the potential well will gain energy at the expense of the radiation. The phase space electrons entering the well with high energy will drop in energy thus amplifying the radiation. Consequently, unless the energy spread of the beam is relatively small compared to the bucket height, the result of the interaction is that the net gain/absorption is severely diminished.

FIG. 12

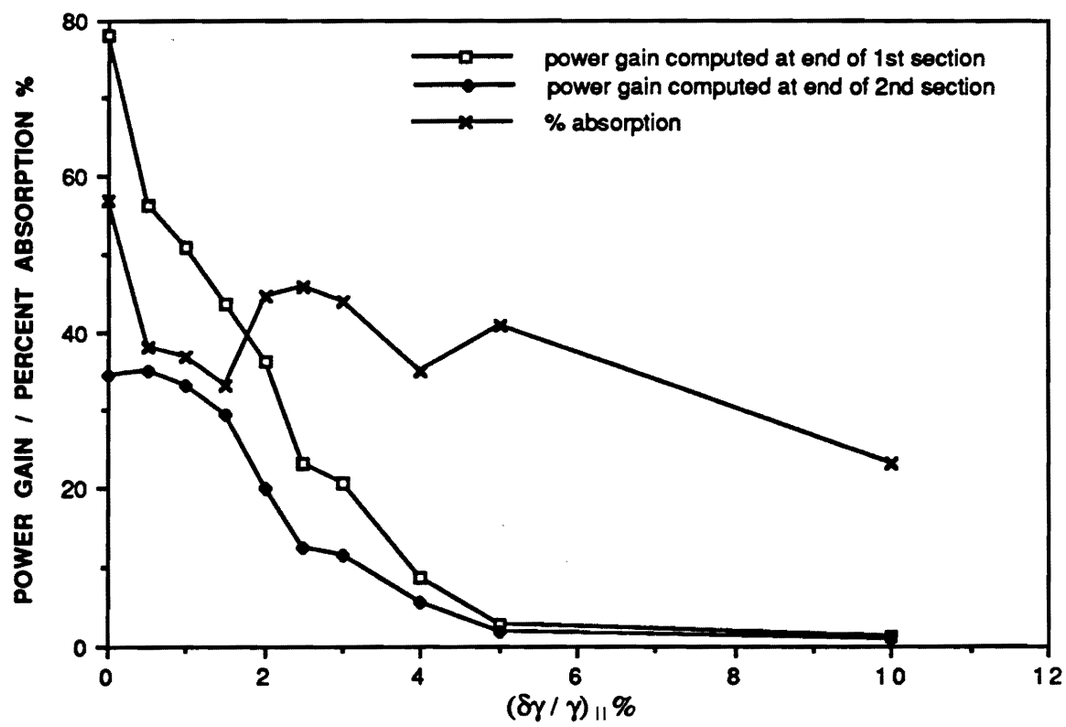

From the plot we see that changes in $(\delta\gamma/\gamma)_{\parallel}$ causes a decrease in the net power output as well as a decline in the overall absorption capability of the IFELA.

2.6 AN ANALYTICAL EXPRESSION FOR A TAPERING PARAMETER WHILE VARYING ONLY $\lambda w(z)$

By using the FEL resonance relation equation (1.1) and applying a number of reasonable assumptions we can generate an analytical expression for a tapering parameter for $\lambda_w(z)$ necessary to give a constant acceleration gradient G. In the following development we make the following assumption; $\frac{d\gamma}{dz} = G = \text{constant} << 1$.

Differentiating equation (1.1) with respect to z we find after cancellation:

$$\frac{1}{\lambda_w}\frac{d\lambda_w}{dz} = \frac{2}{\gamma}\frac{d\gamma}{dz} = \frac{2G}{\gamma}$$

which yields:

$$\lambda_w(z) \cong \lambda_{w0}(1+ \frac{2G}{\gamma_0} z)$$

where we have assumed that terms of order $G^2 \sim 0$ and where γ_0 is the initial value of γ.

For our experiment the actual taper used has a value 0.012 cm^{-1} which is in good agreement with the experimentally obtained average acceleration gradient ~ 6.6keV/cm which gives a value $G \cong 0.013$ and

$$\frac{2G}{\gamma_0} \approx .011.$$

CHAPTER 3

EXPERIMENTAL APPARATUS

3.1 INTRODUCTION

In this chapter we will concern ourselves with the basic Columbia FEL experimental apparatus. Those components which were specially modified or introduced into the system exclusively for the purpose of the IFELA experiment will be discussed in chapter 4.

The operation of any FEL involves a relativistic electron beam and an interaction region where the electrons come under the influence of the undulator. The relativistic electron beam in the Columbia FEL is generated by the Pulserad 220G manufactured by Physics International which is a ~1MeV high field emission pulse line electron accelerator. The accelerator consists of three basic components: 1) A Marx capacitor bank, 2) A pulse forming transmission line and 3) A vacuum diode. The interaction region consists of the main solenoid, the laser resonantor and the undulator. In addition various diagnostics are present which can monitor the diode (i.e. beam) voltage, beam current, millimeter wave power and Marx bank voltage.

Figure 1 is a schematic diagram of the experimental arrangement. The Marx bank develops a high voltage on its end of the transmission line, this voltage serves to charge the transmission line resonantly. When the voltage on the line reaches the proper value the gas switch located at the opposite end of the transmission line closes and

the power on the line is partially absorbed by the load, which is formed by a radial water resistor in parallel with the vacuum diode, located beyond the switch. The transmitted power creates a high voltage potential difference across the diode which remains constant for the duration of the round trip travel time of the high voltage pulse on the transmission line. Electrons are field emitted from a graphite cathode and accelerated across the diode; they then enter the drift tube where they experience the periodic magnetic field of the undulator. Both the diode and the undulator are immersed in a strong magnetic guide field ~1T which acts to prevent the electron beam from diverging under the influence of its own space charge and has the additional advantage of enhancing the transverse motion of the electrons. We now proceed to describe these components individually.

FIG. 1

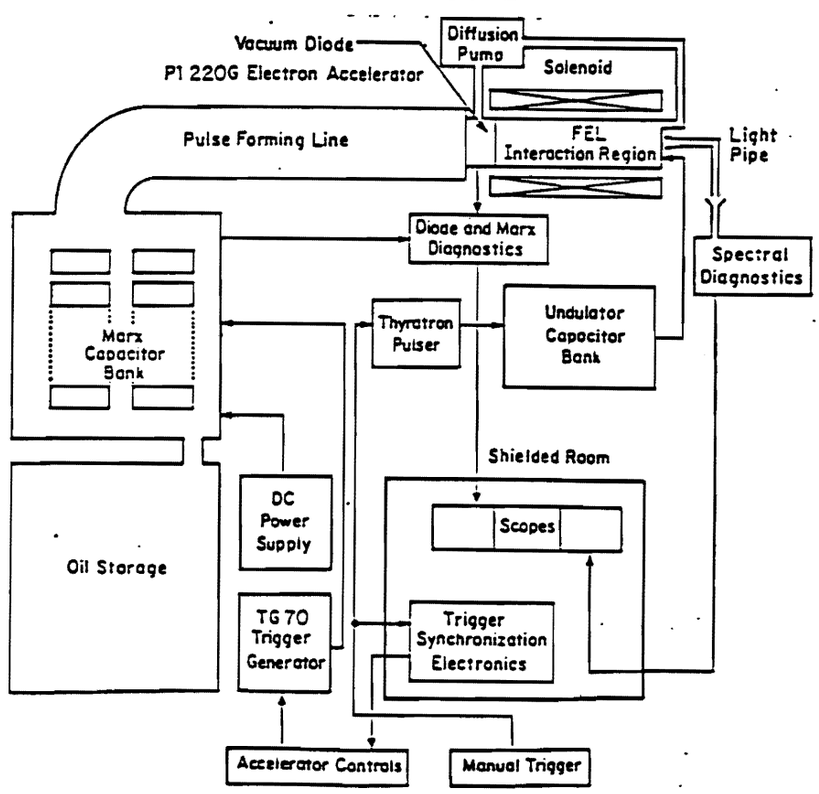

3.2 MARX CAPACITOR BANK

The Marx capacitor bank consists of twenty high voltage capacitors which are immersed in a bath of insulating oil which prevents arcing at high voltages. Figure 2 is a schematic diagram of the Marx bank. The capacitors are charged in parallel, through a series of interleaved water resistors doped with copper sulfate, to the desired voltage ~ ± 40 kV. When the capacitors are fully charged, the marx trigger, which produces a 70kV pulse, is activated to create a spark in every other one of the spark gaps which are located at the midplane between each capacitor. The spark gaps are pressurized with Sulfur Hexaflouride gas which determines the breakdown voltage of the gap and the gas pressure in the spark gaps is regulated externally. The capacitors are connected in series through the spark gaps. On one end of the capacitors in series is a spark gap connected to ground and on the other end is a final spark gap connected to a choke coil which precedes the transmission line.

FIG. 2

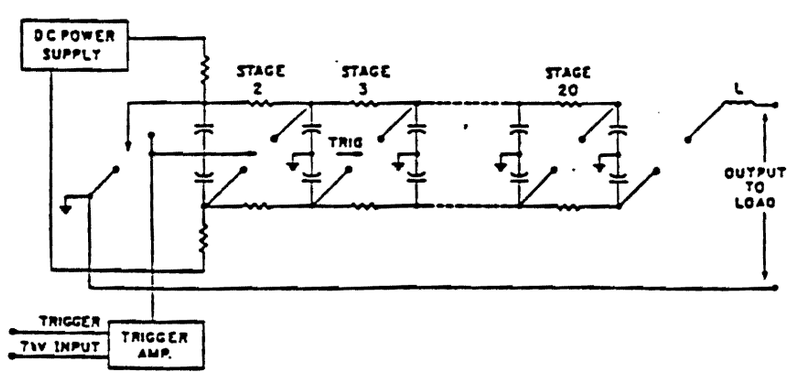

When the capacitors are fully charged the activated spark gaps causes the voltage to double on every other capacitor which results in the overvoltage of the remaining spark gaps and the series discharge of the capacitors. This forms a high voltage (1.6MeV=2 × 20 × 40kV) at the beginning of the transmission line. Figure 3 is an oscilloscope trace of the voltage in the Marx bank as a function of time (time scale: 100 nsec/division)

FIG. 3

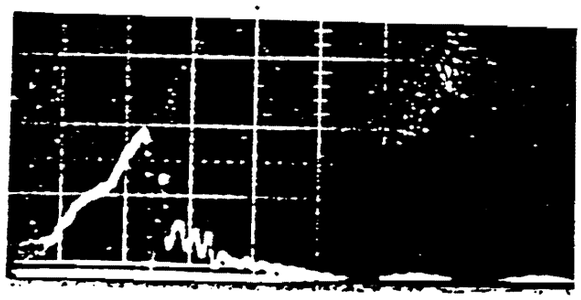

The trace shows that the output Marx voltage grows sinusoidally as the transmission line is charged and then abruptly falls corresponding to the time when the load at the end of the transmission line has drained off the energy. The voltage ringdown at the end of the trace indicates an impedance mismatch at the end of the transmission line.

3.3 TRANSMISSION LINE AND VACUUM DIODE

Figure 4 is a schematic of the transmission line and vacuum diode. The transmission line consists of a 3.7 meter long center conductor

which is tapered and has an average diameter of 10cm, an outer conductor with a constant inner diameter of 60 cm, (the space between the two conductors is filled with ethylene glycol which has a dielectric constant of 40) a gas filled switch, a water resistor and the vacuum diode.

FIG. 4

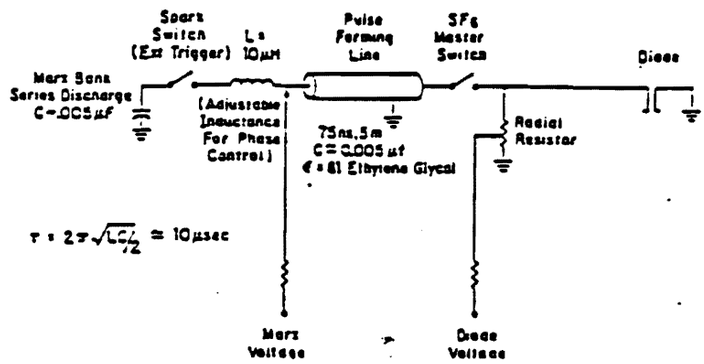

The output voltage from the Marx acts as an ordinary LC discharge and follows the relation:

$$V_{Marx} = V_0[\cos(t/\sqrt{LC})-1]$$

this voltage output is not suitable to drive the electron beam for the FEL where a constant beam voltage is necessary. The transmission line acts to condition the pulse from the Marx to supply a constant potential difference across the diode for ~150nsec.

The output current from the Marx resonantly charges the center conductor of the transmission line. When the voltage on the center conductor reaches the desired value, the gas switch closes and the voltage pulse is delivered to the diode. By properly matching the impedance of the load (i.e. the water resistor in parallel with the

diode) with the impedance of the line, we find according to the equation[29]:

$$V(z,t)=\frac{V_o}{2}\,[U(t-z\sqrt{LC})+\rho_T U(t+z\sqrt{LC}-2t_r)$$

(where U is a step function, $\rho_T=(R_T-\sqrt{LC})/(R_T+\sqrt{LC})$) is the reflection coefficient at the "downstream"end of the transmission line, L,C and R_T are the inductance, capacitance and resistance of the load and t_r is the one way transit time) that the pulse is 50% reflected, resulting in a constant voltage on the cathode (equal to half the transmission line voltage at breakdown) for the duration of the round trip transit time of the reflected voltage pulse which travels backwards along the center conductor and is 100% reflected at the other side of the transmission line.

The gas switch consists of a pair of hemispheric metal electrodes which have a 4 cm separation between them. The breakdown voltage for the SF_6 filled gas switch is determined by the gas pressure in the switch. The pressure is regulated externally and is independent of the gas pressure in the spark gaps located within the Marx bank. When breakdown occurs the switch is closed by the high field emission current which is formed across the electrodes.

The water resistor is a coaxial container of distilled water, 20 liters in volume, which is doped with sodium thiosulphate to give it a conductivity of 170-180 μmhos. The water resistor in parallel with the vacuum diode forms the load at the end of the transmission line.

The resistance of the water resistor is such that it matches the impedance of the load to that of the transmission line. The load dissipates about half the power of the voltage pulse as mentioned previously. The voltage across the diode is monitored by a pair of electrodes located near the rim of the water resistor. Figure 5 is a typical oscilloscope trace of the diode voltage:

FIG. 5

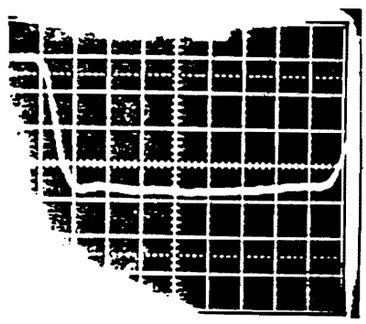

In the trace the diode voltage is measured as a function of time (time scale 20 nsec/division, vertical scale ~200 kV/division). Notice that the voltage rises sharply at the beginning of the trace then maintains a relatively constant value for 150nsec and then terminates abruptly. The deviation of the voltage from a constant value during the pulse should not exceed 2-3%, however in practice generating flat pulses reproducibly has proved to be a difficult task.

Inside the vacuum diode is an aluminium cathode shank 30.5 cm long and 7.62 cm in diameter; this is tapered to a diameter of 2.5 cm and terminates with a reactor grade graphite tip shaped like an oblate hemisphere (see figure 6) designed to produce parallel

electron trajectories on the axis of the diode. On the microscopic level the surface of the graphite is rough. Small radius, microscopic protrusions exist where the local electric field is enhanced greatly. This enhanced electric field on the surface of the protrusions results in the high-field emission of electrons. A few nanoseconds after the initial high field emission the protrusions explode producing a uniform electron emitting plasma over the whole surface of the cathode.

The anode is a conical tapered piece of graphite with a 4mm diameter hole in the center which allows the electrons to pass through it and into the interaction region. Figure 6 shows the geometry of the diode, the calculated equipotential surfaces[30] and the electron trajectories in the diode region. Most of the electrons in the current formed across the diode are intercepted by the graphite anode surface while some fraction pass through the hole in the center. This type of anode is called an "emittance limited anode" as it allows only those electrons with little or no transverse velocity to enter the interaction region.

FIG. 6

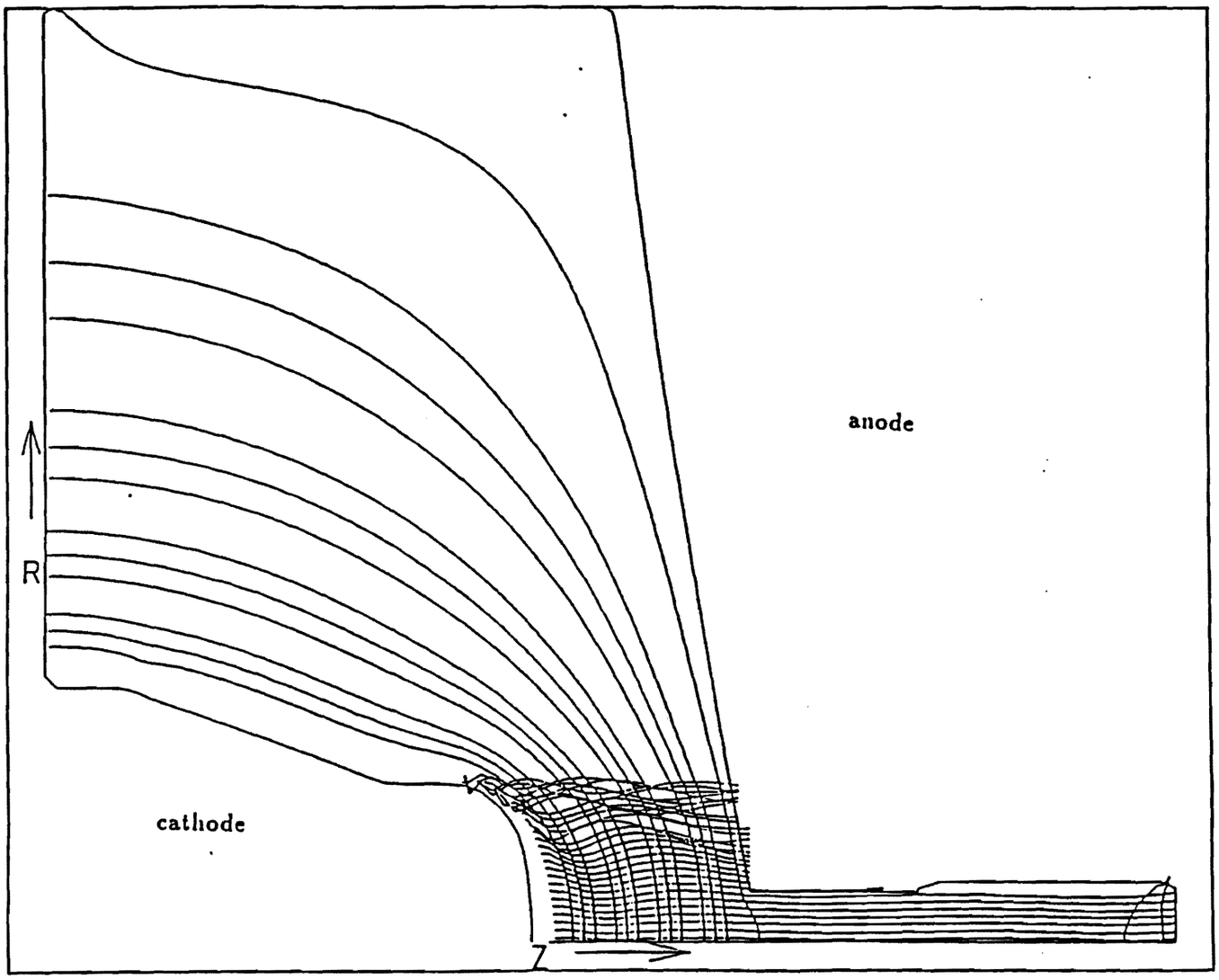

3.4 MAIN SOLENOID

The main solenoid supplies a constant axial guide field in the interaction region. The guide field is produced by a series of 37 stacked copper coils with a total length of 104 cm. Each coil is a single tape-wound solenoid with water channels to allow for cooling.

The coils are connected in series along the electron beam axis. A current of 1500-1600 Amps is supplied to each coil in the main solenoid producing a net field of .95-1.04 Tesla.

As previously mentioned, the guide field acts to confine the electron beam from expanding due to its own space charge field in the interaction region and to enhance the transverse motion of the electrons[31]. The enhancement is a result of the cyclotron motion of the electrons, due to the guide field, being in the same sense as the helical motion induced by the undulator. The effect of this additional magnetic force on the motion of the electrons which changes the effective value of a_w is expressed by the equation:

$$\frac{a_{w(eff)}}{\gamma} = \frac{v_\perp}{v_{||}} \approx \frac{\Omega_\perp}{|\Omega_0 - \gamma k_w \beta c|}$$

where $\Omega_\perp = eB_\perp/mc$ and where $\Omega_0 = eB_0/mc$ where B_0 is the magnetic guide field value. In the absence of any guide field the equation for a_w is:

$$\frac{a_w}{\gamma} = \frac{v_\perp}{v_{||}} \approx \frac{\Omega_\perp}{\gamma k_w \beta c}$$

Thus the effective "wiggler parameter" increases as a result of this "cyclotron" term in the denominator. Care must be taken to to avoid satisfying the resonance condition $\Omega_0 = \gamma k_w \beta c$ because the large transverse electron velocity induced at resonance would cause the electrons to hit the walls of the drift tube thus terminating the

interaction. The actual guide field strength ~ 1 Tesla is far from satisfying the magnetoresonance condition; an enhancement factor of ~2 in a_w is obtained.

3.5 LASER RESONANTOR

Figure 7 is a schematic diagram of the resonant cavity. The dimensions of the resonant cavity are determined longitudinally by two flat mirrors located at each end of the interaction region and radially by the size of the drift tube (inner diameter 1.06 cm).

FIG .7

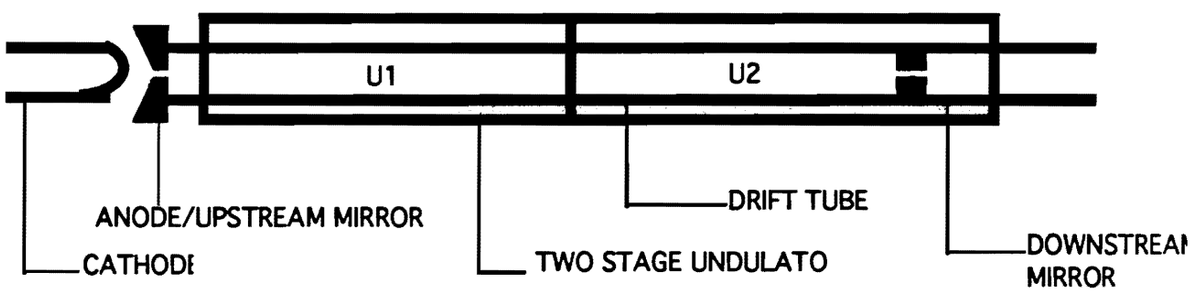

The first mirror, located on the backside of the anode, is a brass reflector with a 4 mm diameter hole in the center to allow for the passage of the upstream electrons. The outer diameter of the first mirror is matched to the inner diameter of the drift tube. The brass in the mirror reflects ≈100% of the radiation incident on it at millimeter wavelengths, It would seem to follow then that the reflection coefficient of this mirror is approximately equal to the

ratio of the brass area to the total area which is ~85%. However it has been found[32] that during oscillation transverse electric field modes set up in the oscillator which minimize the cavity loss. Thus in the case of a hole-centered mirror higher order modes which are null at the center are set up and the actual reflection coefficient is greater, approaching 100%. The downstream mirror is a cylindrical piece of graphite with a 5mm diameter hole in the center to allow for the outcoupling of the radiation as well as electrons. The reflectivity of graphite is ≈100% at millimeter wavelengths, here too the reflection coefficient of the mirror greater than the ratio of the graphite area to the total area which is ~ 75%. We will discuss the properties of this downstream mirror more in chapter 4 when we talk about the electron beam optics of the system. The drift tube is a non-magnetic stainles cylinder having an inner diameter of 1.06 cm and an outer diameter of 1.24 cm.

3.6 DIAGNOSTICS

A set of four diagnostics are present in the system which monitor beam voltage, beam current, Marx voltage and millimeter wave power. In addition pressure valves and gauges are present to regulate the gas pressure in the Marx trigger, the Marx bank spark gaps, and the gas switch located along the transmission line.

The Marx voltage is monitored by an electrode located at the output feed of the Marx bank to the transmission line as in figure 2;

a voltage divider and a series of attenuators reduce the voltage amplitude so that the voltage profile and magnitude can be monitored on the oscilloscope as a function of time. The diode voltage signal obtained from the voltage across electrodes located in the water resistor, is attenuated to yield measurable voltages on the oscilloscope. This diagnostic is calibrated by discharging a 10kV capacitor bank (normally used to drive current through the undulator) on the cathode to ground, through the water resistor, and measuring the resultant voltage across the electrodes. The 10kV capacitor bank itself is calibrated using a precision electrostatic voltmeter. The attenuation factor ~ 10^{-5} is ratio of the measured voltage to the actual voltage across the diode. Obtaining an accurate value for the attenuation factor and therefore the accurate value of the diode (i.e. initial beam) voltage is important in our experiment since we are primarily interested in the energy gained by the electrons during the acceleration process. The total electron beam current is determined by integrating the signal from a loop of wire surrounding the diode gap which monitors the azimuthal magnetic field from the diode current. The current in the beam that actually passes through the anode and into the laser resonator has been measured using a Faraday Cup[33] placed inside the drift tube.

The millimeter wave power output of the FEL is detected by a Schottky-barrier diode positioned along the beam axis. The voltage response of this detector at a 1.5 millimeter wavelength is ≈0.1 Volt/Watt and the characteristic time response is 50-100 psec. The detector will saturate and can even be damaged, if the incident signal

power causes the output voltage of the detector to exceed 500mV. Hence, the detector is used in conjunction with attenuators in the form of cardboard index cards 12.5 cm × 20 cm which reduce the intensity (for millimeter wavelengths) by a factor of ~ 2 for every 17 cards.

All the diagnostics mentioned in this section are connected by 50 Ω coaxial cables, which are enclosed in a copper braiding, to the oscilloscopes. The oscilloscopes are located in a screen room, which shields the scopes from unwanted electromagnetic noise during operation of the FEL, the room is located adjacent (~3m) to the FEL.

CHAPTER 4

IFELA EXPERIMENTAL SETUP

4.1 TWO STAGE REVERSE TAPERED UNDULATOR

Central to the operation of any FEL is the undulator which supplies the periodic magneto-static field experienced by the electrons. Before we discuss the unique undulator design used in the IFELA experiment we proceed to describe the manner in which the undulator operates in the Columbia FEL.

As mentioned in chapter 1 the type of undulator used in the Columbia FEL is helical. It is made from a bifilar helical winding of copper wire 2.1 mm in diameter (12AWG) set in grooves and wrapped around the axis of the drift tube. The grooves are cut by a lathe into an insulating phenolic tube, which snugly fits as a sheath surrounding the drift tube. The two leads emanating from the drift tube are connected to a 10 kV_{max} high voltage capacitor bank. The current is driven through the undulator by first triggering a thyrotron which acts to close the circuit connecting the capacitor bank and the undulator forming an LC discharge. This discharge produces a sinusoidal current in the undulator which decays in time due to the inherent resistance in the circuit. The half period of this sinusoidal current is $\pi\sqrt{LC} \sim 30$ μsec. The electron beam is fired as the current in the undulator, and thus the $B_\perp$ field on the axis, reaches a maximum. Figure 1 is a trace of the undulator current

(bottom trace) and the diode voltage (top trace) as a function of time (time scale 5 μsec/division):

FIG. 1

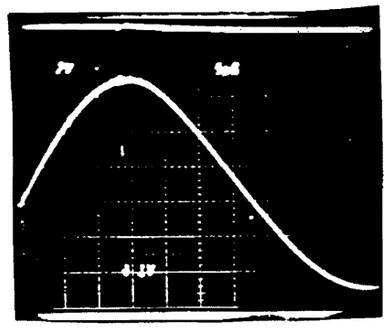

The "spike" in the center of the trace is the diode voltage it follows the triggering of the Marx bank which itself occurs 15 μsec after the beginning of the LC discharge. This time delay is obtained using a digital time delay unit located in the screen room.

The undulator used in the IFELA experiment consists of two sections. The first section has a constant period λ_w = 1.43 cm and has a length of ~41 cm. At the beginning of this first section the radius of the windings has a value of 3.1 cm and is tapered for the first ~11 cm until it reaches a final constant value of 2.3 cm. The need for this adiabatic entry region is to insure that the electron beam is not subjected to a sudden change in the magnetic field as it enters the undulator. Exposing the beam to a sudden change in the $B_\perp$ field results in an unacceptably large emittance of the electron beam. Figure 2 is an experimental plot of the transverse B field on axis at the entry to the first section of the undulator.

FIG. 2

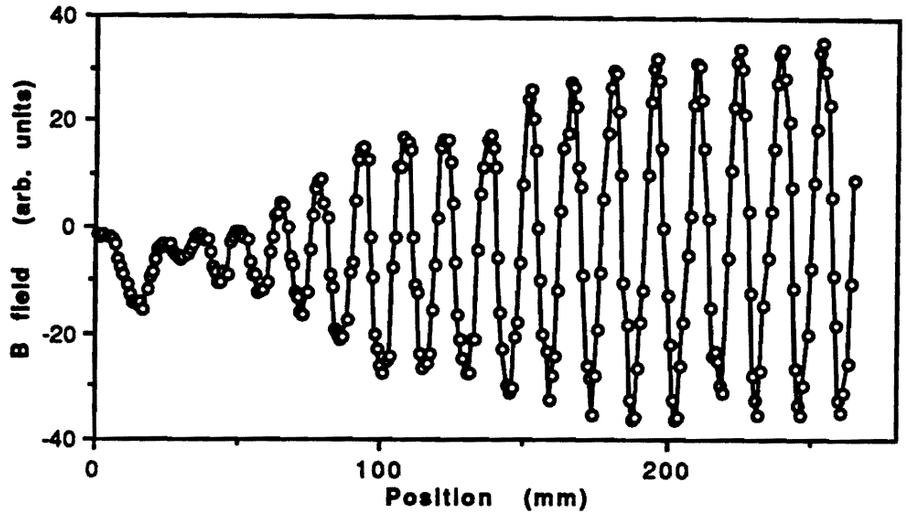

Measurements of the magnetic field in the undulator were performed using a multiturn B-dot loop located at the end of a glass tube 66cm long. The normal to the plane containing the area of loop is placed perpendicular to the beam axis. Discharging the undulator capacitor bank repetitively, at low voltages, as the probe is moved axially along the undulator allows for the measurement of the relative field values along the undulator axis. The B-dot loop is calibrated by using a Helmholtz coil with a known current to obtain absolute values for the magnetic field. This allows for absolute magnetic field measurements on the axis of the undulator. For such measurements the voltage on the capacitor bank is set at the value actually used during the experiment.

The second section of the undulator has a "reverse tapered" period beginning at λ_w = 1.8 cm and continuing for ~38 cm to a final

value of 2.25 cm. The tapering parameter is thus $\frac{d\lambda_w(z)}{dz} = 0.067$. Figure 3 is an experimental plot of the transverse B field in the second section:

FIG. 3

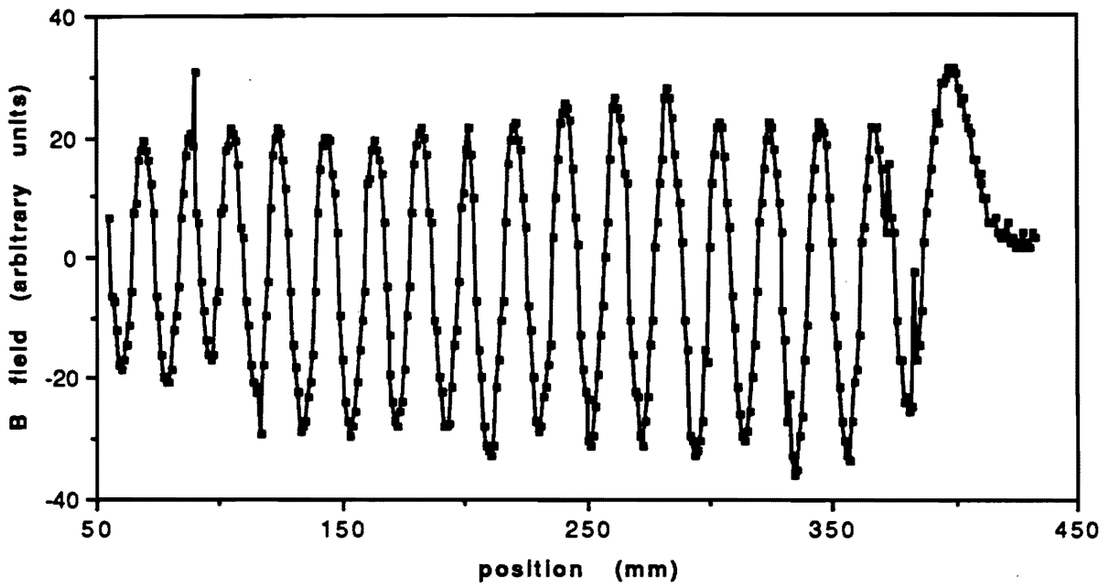

In the figure we see that the spatial period of the transverse B field grows along the axis. It is apparent that the value for the maximum transverse B field on the axis also varies; this variation in the field amplitude in the second section was mathematically modeled and was input into the numerical simulation. The resultant signal absorption and electron energy spectrum was found to be insignificantly different when compared to the case where the $B_\perp$ field in the second section was kept constant.

The undulator is wound with two separate bifilar copper windings. One wire is wound along the entire length of the undulator producing a transverse B field in both sections while a second winding extends only for the length of the second section. The purpose of this secondary winding is to provide an opposing current in the second section which can cancel the transverse field in that section. The cancellation of current was achieved by placing an inductive load in series with the secondary winding to match the inductance of the primary winding, therby matching the phase and magnitude of the current in both windings. However it was found, during the measurement of the B field in the second section, that although the currents in the primary and secondary windings were equal and opposite the resultant transverse B field on axis was not zero. This nonzero result for the transverse B field is due to exponential dependence of the B field on the radius of the windings surrounding the undulator. This radial dependence follows the relation[34]:

$$B_{\perp}(\text{on axis}) = \frac{4\pi^2}{5}\frac{I_w}{\lambda_w}\sqrt{\frac{a_0}{\lambda_w}}\, e^{-2\pi a_0/\lambda w}$$

Where a_0 (=1.45 cm) is the radius of the winding and I_w is the current in the windings. For our undulator the difference in radial length for the two windings is just equal to the diameter of the copper wire 2.1 mm. Using the above relation and substituting in the experimental values for λ_w and a_0 we find that the transverse B field value on axis is diminished by a factor of ~ 5/8 in the case where equal and opposite currents are driven through the two

windings as opposed to the case with zero current in the secondary winding. When we substitute the the experimental value for Iw in the case of opposite currents we find a field on axis of 250G. In chapter 2 section 4 we discussed the effect of lowering the B field (B=250) present in the accelerating section in the numerical simulation and found that the effect was to accelerate fewer electrons than the higher field case (B=400G). When we look at the experimental data in chapter 6 we will see that this effect is seen experimentally as well.

The secondary windings can also be "crowbarred" resulting in an opposing image current in this winding which diminishes the transverse B field on the axis in the second undulator section. Table 1 shows the values for the maximum transverse B field in the first and second section as the configuration of the secondary windings is changed.

TABLE 1

Config. of Secondary winding	$B_{\perp max}$ in 1st sect.	$B_{\perp max}$ in 2nd sect.
Cancelling Current	650G	250G
"Crowbar" Current	620G	400-480G
No current in second winding	675G	850G

The experimental values in Table 1 were obtained using the method for determining the absolute value for $B_{\perp}$ on the axis. The voltage on the undulator capacitor bank used when making the

measurement was 4.4 kV which was also the value used while running the experiment. In what follows we will refer to the crowbarred configuration of the secondary winding as the HiB mode and the case where an opposing current is driven through the secondary winding as the LoB mode.

Fabrication of the two stage IFELA undulator proceeded as follows: The first section with the constant period λ_w=1.43 cm was cut on a lathe with the cutting tool advancing at the appropriate rate so as to cut grooves at the proper period. The depth of the grooves at the beginning of the first section of the undulator is 0.5 cm and is tapered to a final depth of 1.1 cm; the approriate depth is reached by repeatedly operating the lathe with the cutting tool advancing radially by ~50/1000 inches each time while starting to cut further down the undulator axis to achieve the taper in the groove depth. Two seperate helices were cut, 180° apart. For the second section however the task was not so simple since the period of the grooves changes as a function of position. A computer printout of a helix was generated with the actual scale reverse tapered period. The printout of the period was wrapped around the remaining uncut section of the phenolic tube. The grooves were then cut by hand along the printout in order to finish the second section of the undulator.

4.2 MAGNETO-OPTIC ELECTRON TRANSPORT AND MAGNETIC SPECTROMETER

The main purpose of the IFELA experiment was to observe the phenomenon known as stimulated absorption. Stimulated absorption in the FEL involves the absorption of power from the radiation field and the transfer of absorbed power to the electrons thus increasing their kinetic energy. We detect this phenomenon in two ways. First, the power output of the IFELA is monitored, to look for the absorption of radiation, using the Schottky-Barrier diode. Secondly, we monitor the energy of the electrons exiting the IFELA, using a mass spectrometer which spatially resolves the electrons according to their energy. In this section we will describe the electron transport system and in particular we will describe the characteristics of the mass spectrometer. Detection of the electrons which are spatially resolved according to energy by the mass spectrometer will be treated in the next section.

The experimental values of the parameters used (i.e. field strength, length and orientation) in the magneto-optic elements comprising the electron transport system were obtained using the TRANSPORT© computer code[35]. The code characterizes the electron beam as a 6×6 matrix and determines the beam's trajectory as it encounters various magnetic elements (i.e. quadrapole, dipole, solenoid, free space...) in its path. The various magnetic elements are represented by matrices and the code successively multiplies the beam matrix with these magnetic element matrices. The output of

the code gives: 1) The spot size of the beam in the x and y direction in the plane perpendicular to the beam 2)The angular divergence of the beam in the x and y direction and 3) The pulse length of the beam (not of interest in our case), following each successive magnetic element.

Before building the magneto-optic assembly, an experiment was performed to determine how the electron trajectories were affected by the fringing fields present at the exit from the ~1T main solenoid, on the beam axis. This is also the location of the downstream mirror of the resonant cavity and this electron outcoupling mirror forms the objective for the electron beam optics which follow. A homemade electron gun ~200V was placed at the exit of the main solenoid in an evacuated glass cylinder centered on the solenoid axis. The residual gas in the tube, which was fluorescent, allowed for viewing of the electron beam trajectory at this location. It was found that, upon exiting the solenoid the electron beam was deflected upward from the axis and that the beam diverged a few centimeters after the exit along the fringe field of the main solenoid when the solenoid field was at its full operating value of ~1T.

To correct for this deflection and divergence of the beam, and to transport the beam to a region where the fringing field of the main solenoid was negligible a small focusing solenoid was placed immediately following the main solenoid. The length of this focusing solenoid was 17 cm and its field strength during operation was ~1kG. This solenoid was wound with copper wire 1.55 mm diameter

(14AWG) which was wrapped around a spool cut from the same phenolic used in the undulator and fit over the section of drift tube extending beyond the interaction region. The solenoid was powered by an LC circuit with a half period of ~700 μsec. The discharge in the LC circuit was initiated 350 μsec prior to the discharge of the undulator capacitor bank so that the electrons experienced the maximum focusing field as they traverse the focusing solenoid. The 350 μsec delay was accomplished using a separate time delay unit located in the screen room. Inside the drift tube, at a position corresponding to the beginning of the focusing solenoid, is the cavity downstream mirror which is a small cylinder of polished graphite with a 5 mm hole in the center. This graphite cylinder acted as an electron beam aperture which formed the objective for the beam optics located beyond the interaction region. Figure 4 is a schematic diagram of the focusing solenoid and the mass spectrometer.

FIG. 4

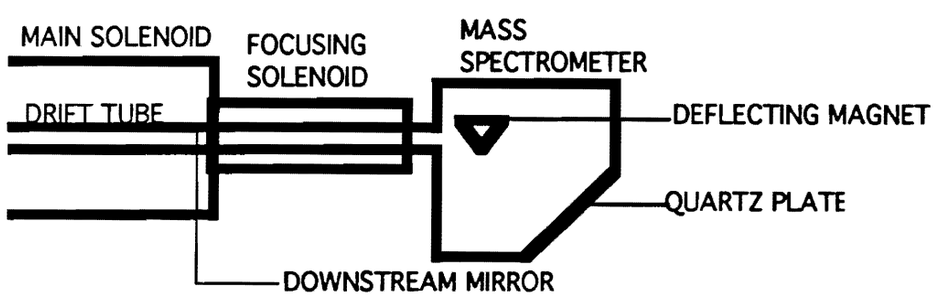

The mass spectrometer chamber fits directly onto the end of the drift tube. A gap of length 6 cm existed between the downstream end of the focusing solenoid and the entrance to the chamber. A thick (i.e. 4mm) Polyethylene plug having an axial aperture 3.8 mm in

diameter was placed on the beam axis located at the entrance to the mass spectrometer. The choice of polyethylene was made since this material will intercept the electrons but will not attenuate the millimeter power output of the IFELA. The effect of this polyethylene electron beam aperture was to reduce the beam current space charge entering the mass spectrometer and thus reduce the electron beam spot size on the focal plane. A small spot size was crucial in achieving satisfactory electron energy resolution.

Immediately following the polyethylene plug the electrons come under the influence of a vertical dipole field of adjustable size ~350-600G, which caused the electrons to be deflected by an angle θ from their initial direction. θ is related to the electron energy and the strength of the deflecting field by the following approximate relationship:

$$\theta = \frac{2eB_{\perp}d}{\pi\beta\gamma mc^2}$$

Where d is the length that the electrons are exposed to the deflecting field. The deflected electrons are focused onto a 12cm $\times$ 3cm $\times$ 3mm optical quality quartz plate which is coplanar with the focal plane. The index of refraction of the quartz is n ~1.53 and the electrons upon hitting the quartz plate produce C'erenkov light. The choice of quartz was made due to the high yield C'erenkov photon production for that material[36]. The inner side of the quartz plate was coated with a thin film of graphite which prevented light not produced by the energetic electrons from being detected on the other side of the

quartz. The graphite coating also prevents electrostatic charge buildup on the quartz plate.

A circular 2.54 cm diameter, thin, polyethylene window was built into the mass spectrometer chamber. It is located in the line of sight of the electron beam and permitted monitoring of the output power level during operation of the IFELA. A scale diagram of the mass spectrometer including dimensions is presented in figure 5.

FIG. 5

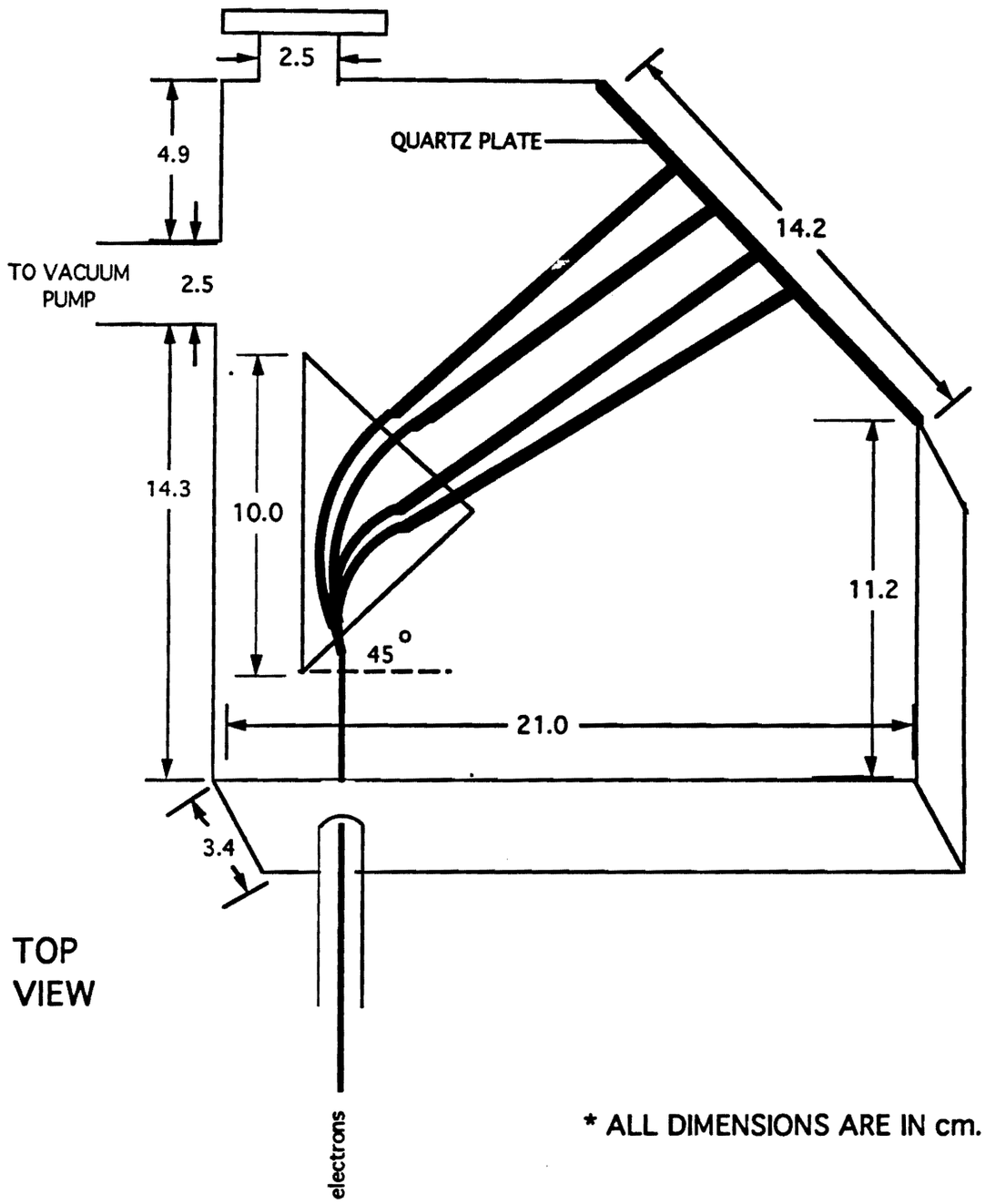
2.5
4.9
QUARTZ PLATE
14.2
TO VACUUM PUMP
2.5
14.3
10.0
11.2
45°
21.0
3.4
TOP VIEW
electrons
* ALL DIMENSIONS ARE IN cm.

The vertical deflecting field experienced by the electrons upon entry into the spectrometer chamber is supplied by a dipole magnet. The poles are separated by a distance equal to the thickness of the spectrometer chamber. Initially a circular geometry was used for the polefaces; however after it was found that the resultant spot size of the beam on the focal plane was unsatisfactorily large, the TRANSPORT code was consulted and the shape of the pole faces was changed to a triangular geometry. The electrons now entered the deflecting field at a 45^0 angle and exited roughly normal to the field as in figure 5. The core of the dipole magnet was a 6.35 cm diameter cylinder made of iron with a high magnetic permiability (i.e. high μ). The iron was wrapped with 5 layers of 1.55 mm diameter copper wire (14AWG) yielding a winding density of ~32 wireturns/cm.

The current in the copper wire was supplied by a homemade 15V power supply. The power supply plugs into the wall voltage (120 V). A variable transformer (Variac) was used to adjust the wall voltage which served as the input voltage on an 8-1 high power stepdown transformer. This low AC voltage was then converted to DC using a high power bridge rectifier mounted on a heat sink. The dipole field resulting from the DC current in the wires was measured as a function of variac settings on the power supply. No cooling mechanism was employed to remove excess heat from the dipole magnet, so to prevent overheating, the power supply was set to a predetermined variac setting and switched on remotely, prior to each firing of the electron beam, from the control area.

4.3 DETECTION OF C'ERENKOV LIGHT PRODUCED BY SPATIALLY RESOLVED ENERGETIC ELECTRONS

The quartz plate which lies on the focal plane of the electrons passing through the mass spectrometer constitutes a "thick C'erenkov target". This means that due to the multiple collisions experienced by the energetic electrons entering the quartz, the emitted C'erenkov light does not exit the quartz at the C'erenkov angle $\theta_c = \cos^{-1}(1/n)$; (valid if the electrons are not deflected from their original trajectories) rather the light exits in the forward direction through the non-vacuum side of the quartz. The emitted C'erenkov light forms the object for an optical arrangement of mirrors and lenses which forms an image of this light on the light sensitive surface of a Photomultiplier tube located in the screen room. Figure 6 is a schematic diagram of the optical arrangement used to detect the electrons impinging on the vacuum side of the quartz plate.

The output signal from the Photomultiplier is directly proportional to the light intensity incident upon it. The intensity of the light is directly proportional to the number of photon producing electrons hitting the quartz at the object position of the optics. Thus the output signal from the photomultiplier provides a direct measure of the number of electrons hitting the spot on the quartz which forms the object of the optical system.

The optical detection arrangement was configured in two ways. In the first configuration a single optical channel is monitored. Initially

the light spot, caused by the electron beam, is found as a function of position along the quartz. To accomplish this initial detection the undulator field is turned off and the deflecting field is set at the optimal value to achieve a minimum spot size. Once this initial calibration is achieved the optics are then focused on this location and the photomultiplier signal is recorded for a beam passing through the IFELA with the undulator turned on. By changing the field strength of the deflecting magnet electrons possessing different energies can be focused into this single optical channel. The relative populations of electrons possessing different kinetic energies can then be measured during operation of the IFELA. These relative populations are plotted to yield a normalized electron energy

FIG. 6

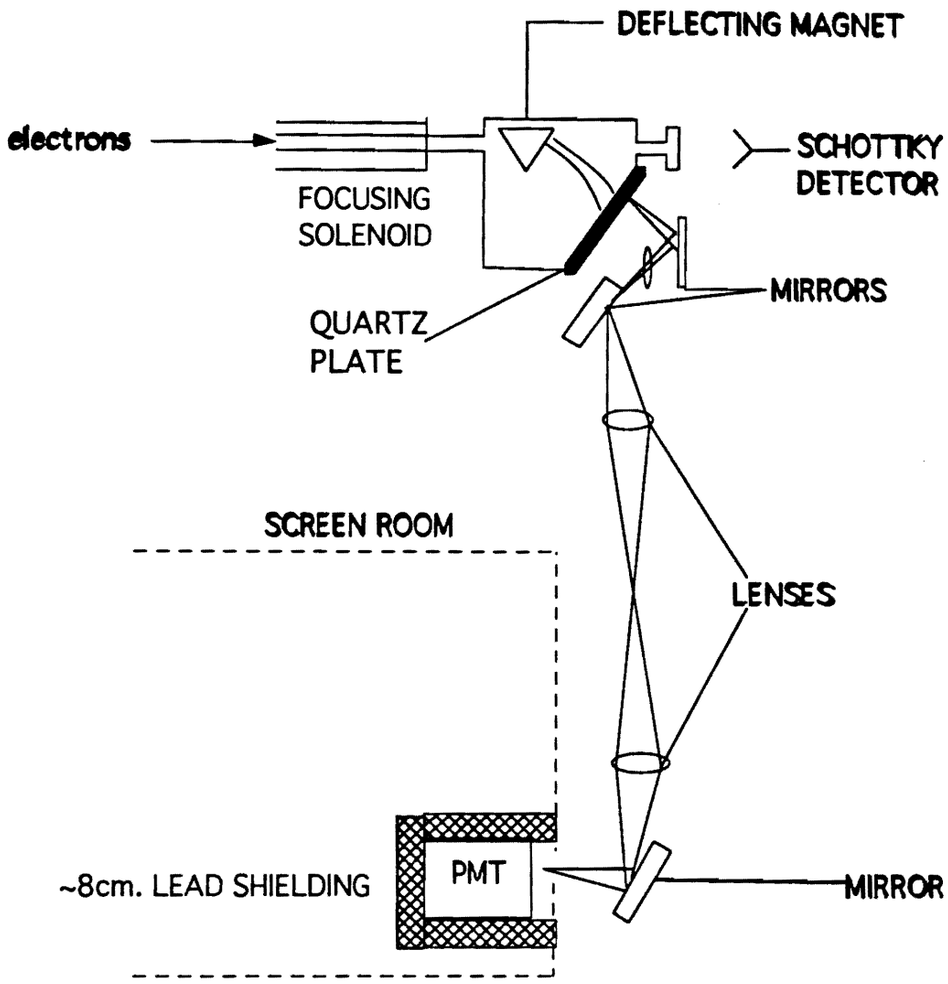

spectrum. The energy resolution of the (mass spectrometer/optical detection) system is characterized by: a) the spot size of the beam on the focal plane and b) the resolving power of the optics, which determines the width of the optical channel. In sect 4.4 we will discuss the spatial/energy resolution of the combined system quantitatively.

In the second configuration two separate optical channels are monitored simultaneously. Light from both optical channels is reflected from the same mirror. The light from each source is then focused by two separate series of lenses and imaged on the two photomultipliers located in the screen room. The initial object separation of the light sources on the quartz 3 cm is enlarged by the optical system giving an image separation of 15-20 cm so that each image is formed on its own photomultiplier. The benefit derived from using this configuration is that it provides for a more exact experimental verification of theoretical predictions, since two points on the electron energy spectrum can be plotted simultaneously for their relative populations during a single operation of the IFELA. In particular verification can be made of the existence of the "valley" in the electron energy spectrum (see Chapter 2 Figure 3) between the group of electrons accelerated to energies with $\gamma \sim 3$ and those electrons downshifted in energy from their initial value where $\gamma \sim 2.5$.

The voltage on the photomultiplier used during the experiment was 1750V. No sources of illumination were allowed in the experimental area during the experiment thus insuring the integrity of the photomultiplier signal. The photomuliplier itself is shielded with a ~8 cm layer of lead on all sides with a 2.5 cm hole directly in front of the photomultiplier lens to transmit the light from the quartz. In the experimental area, during operation of the IFELA, there is an abundant amount of x-ray radiation. The lead shielding

prevents the x-rays from reaching the photomultiplier, thus eliminating x-ray noise from the photomultiplier signal.

4.4 CALIBRATION AND ENERGY RESOLUTION FOR THE MASS SPECTROMETER/OPTICAL DETECTION SYSTEM

A novel method was devised to directly measure the location of the light spot, caused by the electron beam, on the quartz . An oscilloscope camera was mounted directly onto the quartz plate. The film in the camera, Polaroid 612, is highly sensitive and becomes exposed by a light signal of only a few nanoseconds in duration. By opening the camera shutter and blocking out all external light sources, a time integrated photograph of the light spot formed on the quartz plate is obtained. Figure 7 shows a series of actual size spectrographs taken at a fixed electron beam energy with different values for the deflecting field in the mass spectrometer. The white lines running through the figure denote the horizontal edges of the quartz plate that can be viewed through the spectrometer. In the vertical sense the photographs show that the spot moves along the lower edge of the quartz window.

FIG. 7

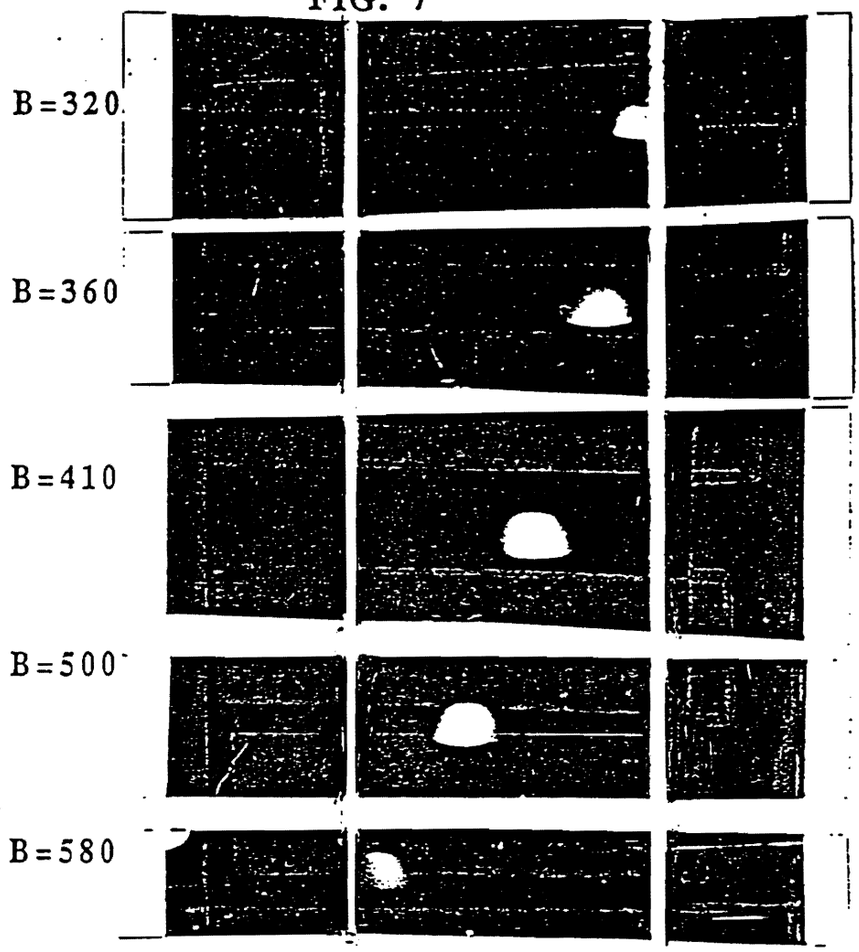

Figure 8 is a plot of the calibration data taken from a group of spectrographs where the beam energy and the value for the deflecting field was varied. The x axis represents the location of the spot along the quartz as seen on the spectrograph and the y axis is the B/γ value (which is proportional to θ) used while taking the spectrograph.

FIG. 8

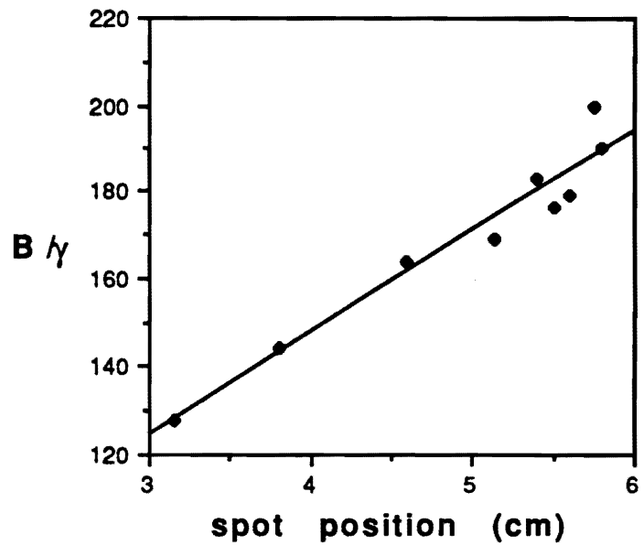

The spot size on the focal plane changes both as a function of the deflecting field in the mass spectrometer and the electron energy. The maximum light spot diameter able to be imaged by the optics is =1 cm. The photomultiplier signal is normalized to account for the broadening of the spot size at different energies. By using the direct photographic method we can measure the spot width for a given group of electrons. If the width of the spot size, for a group of electrons possessing a given energy passing through a given deflecting field B_d, is X cm then the photomultiplier signal is multiplied by a factor of X to correct for the lost C'erenkov light which is not collected by the optics. The minimum spot size achieved for those electrons possessing an energy equal to the injection energy, at the optimal value for the deflecting field at that energy is ~1 cm, so the photomultiplier signal for electron having these parameters requires no correction. Figure 9 is an experimental plot

of the horizontal spot width of the electron beam on the focal plane as a function of deflecting field for the same electron energy (i.e. E ~ 750keV); also plotted is the theoretical spot size obtained using the TRANSPORT code.

FIG. 9

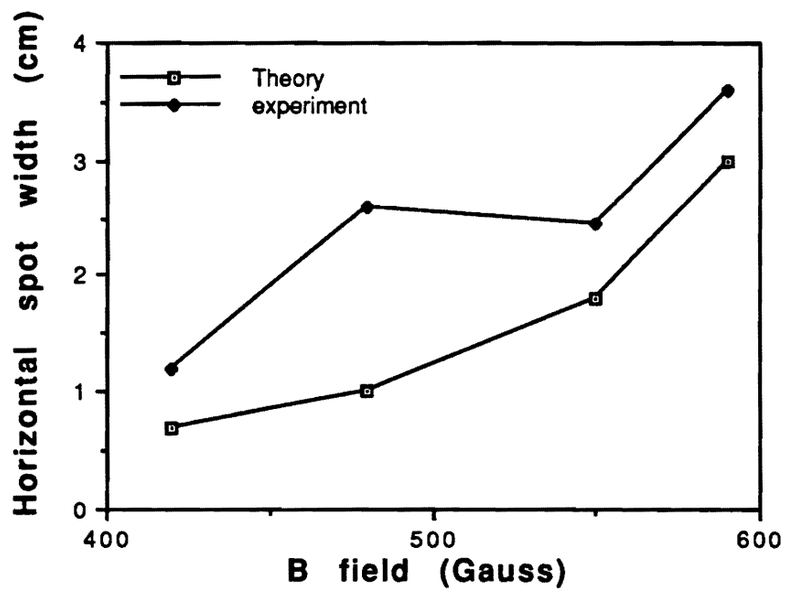

Alignment of the optics was accomplished by placing an incandescent flashlight bulb at the location of the optical channel, determined using the above mentioned photographic method, and adjusting the optics to produce an image of the light from the bulb on the face of the photomultiplier tube.

For the second optical configuration, where two optical channels are monitored simultaneously, the minimum allowed separation of the channels is limited by the width of the spot size for each electron energy being monitored. In the actual experiment it was found that

satisfactory resolution was insured only when the separation of the channels was at least 3 cm; this distance was also the minimum separation necessary to avoid crosstalk between the two optical systems which transport the light emitted at each channel. Relative calibration of the photomultiplier tubes was necessary since the signals from the photomultipliers were compared to determine relative electron populations at different energies. The photomultipliers were calibrated by exposing each one to the identical light source (i.e. the flashlight bulb with the same batteries) located at its own object position on the quartz and measuring the resultant signal for each one. During the calibration procedure the incident light was chopped to avoid saturation of the photomultipliers.

CHAPTER 5
DATA COLLECTION

In this chapter we present a chronology of the different stages in the IFELA experiment and how data was collected. A detailed description of the criteria which must be met to insure proper data selection as well as the methods employed for the interpretation of the data are also discussed.

5.1 PRELIMINARY EXPERIMENTAL FINDINGS

The experimental work, as well as the data collection, presented in this section was performed by my colleague Yung Ping Chou, who conducted the initial phases of the IFELA experiment. Mr. Chou was responsible for the fabrication of the undulator as well as its installation on the beamline. There were several constraints imposed by the nature of the experimental apparatus that went into the design 1) The total length of the undulator could not exceed 80cm (the length of the main solenoid) 2) It was necessary that the period in the second section section of the undulator not approach the magneto- resonance value ($\lambda_W \cong 3$ cm) for a guide field value of 9.45kG. It was found that a cancelleling current was necessary to diminish the magnetic field strength in the second section of the undulator. In the absence of any cancelling current the electron beam is deflected into the walls of the drift tube upon suddenly encountering a large change in the magnetic field (from ~600G to1000G) in the second section. Mr. Chou's comments, suggestions

and preliminary work on the IFELA experiment are greatly appreciated.

The method initially employed to look for signs of stimulated absorption was to monitor the output millimeter wave power of the IFELA to look for signs of absorption in the power profile in the vicinity of the resonant (i.e. design) energy. In figure 1 we see two oscilloscope traces of the power signal. Figure 1a is a signal profile taken with the magnetic field in the second section partially cancelled, while figure 1b was taken when the value of B in the second section was at its higher value, where significantly more absorption is expected.(time scale 20nsec/div)

FIG. 1

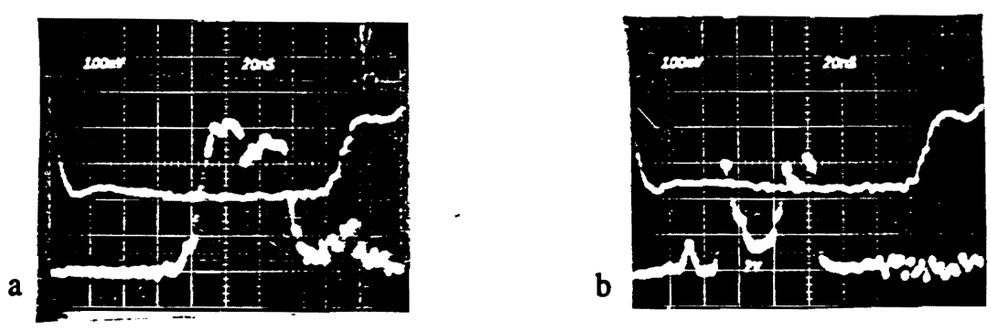

Notice that in figure 1b there is a sudden drop in the power output in contrast to figure 1a where the power profile remains relatively constant. This dip in power output was tentatively attributed to the absorption of radiation occurring in the second section of the IFELA undulator. Furthermore it was found that the integrated total power output from the IFELA undulator configuration was roughly 50% less, on average, than the total power

the Columbia FEL[19]. These conclusions were arrived at after a large number of power profiles in each undulator configuration were examined and a consistently lower value for the total outputpower was found in the case of the IFELA.

As mentioned in chapter 1 the first section of the undulator together with the mirrors in the resonant cavity function as a conventional FEL. The power generated by the first section of the undulator in the IFELA has a frequency spectrum identical to the spectral output of a conventional FEL. In a conventional FEL the power is spectrally distributed among several wavelengths. The majority of the power resides in what is called the "carrier" wavelength, however a significant portion of the power (up to 1/3) can be found at the "sideband" wavelengths. In general, the sidebands have wavelength values which differ from the carrier wavelength by 5 -10%[26].

It was found that for the IFELA undulator operating with an electron beam energy of 750 keV the carrier wavelength is λ_s=1.65 mm the upper sideband wavelength is λ_s~1.79 mm and for the lower sideband λ_s~1.48 mm. These spectral measurements were performed using a reflection grating, millimeter wave, spectrometer located in the experimental area downstream from the FEL.Figure 2 is an experimental plot of the power level located at the carriers as well as sideband wavelengths for the case of both the high and low magnetic field in the second undulator section.

FIG. 2

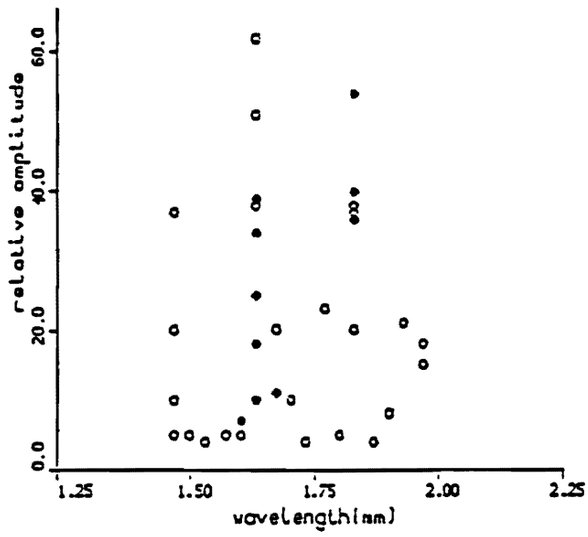

O-WITHOUT 2nd SECTION
●-WITH 2nd SECTION (TAPERED)

The data in figure 2 suggests but not conclusively that the sidebands remain unaffected by the acceleration process.

5.2 OVERVIEW OF DATA COLLECTION

After successful detection of stimulated absorption as evidenced by the diminished power level observed during operation of the IFELA the next stage of the experiment called for direct measurement of the energy spectrum for those electrons exiting the IFELA. As mentioned in the preceeding chapter, experiments as well as numerical studies were conducted to aid in the construction of a magneto-optic arrangement including a mass spectrometer. Following a check for effective beam transport (i.e. to the quartz window) and the subsequent calibration of the mass spectrometer a data run

magneto-optic arrangement including a mass spectrometer. Following a check for effective beam transport (i.e. to the quartz window) and the subsequent calibration of the mass spectrometer a data run commenced using the single optical channel configuration for the optical detection system. After a prolonged hiatus in data collection, caused by poor power production, a second data run began using the second optical configuration which involves the monitoring of two separate optical channels. The motivation for using this second optical configuration was that some of the features of the predicted energy spectrum could be verified with greater certainty by simultaneously monitoring two separate groups of electrons possessing different energies. A final data run using the two channel configuration was done following a second break in data collection due to required system maintenance. Sample data from each data run and comments regarding the relative characteristics and quality of data from each run are presented in the next section.

5.3 SAMPLE DATA

I. The first data run, which was conducted while monitoring a single optical channel, yielded a significant amount of interesting data. During the run the measured power output for the IFELA was, on average, 400-600mV which corresponds to a 4-6 MW maximum value for the actual power. Flat (i.e. constant value) diode voltages at the resonant (design) energy value were also achieved rather consistently. Figures 3a-e contain two exceptional examples of power absorption and the consequent electron acceleration collected during this first data run.

FIG. 3

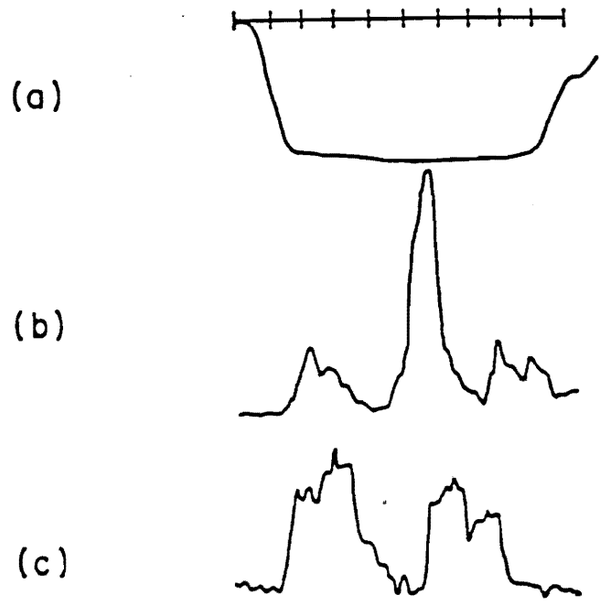

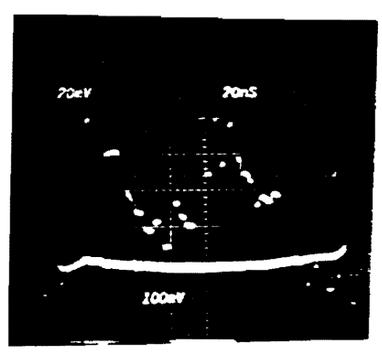

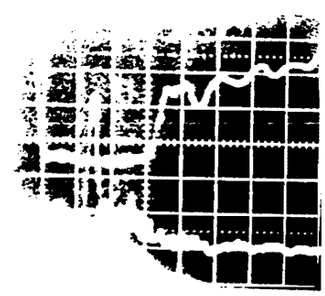

Figures 3a-c (time scale 20nsec/div) were all taken during a single shot of the electron beam and the traces are synchronized in time. Figures 3a are diode voltage traces (note the nearly constant value of the voltage for the full 150 nsec duration of the electron beam). The voltage (i.e. vertical) scale in figure 3a represents an actual voltage value of ~750 keV for the injected beam which is the

resonant value for the beam energy according to the design. Figure 3c is the output power profile from the IFELA as measured by the Schottky diode (17 index cards were placed in front of this detector thus attenuating the intensity of the incoming signal by a factor of 2). Notice the dip in the middle of the trace indicating the sudden absorption of radiation. It should be noted that in this figure the absorption is ~ 100% indicating that all of the power (both the carrier as well as sideband radiation) is absorbed contary to our assertion that the sidebands remain unaffected by the absorption. However if we recognize that the sidebands do not necessarily maintain constant power for the duration of the pulse then this total power absorption is not anamolous. Figure 3b is a trace of the photomultiplier signal with the optical detection system focused at a position corresponding to ~1MeV electrons, well above the injection energy value. Note that the "spike" in the photomultiplier signal occurs ~30nsec following the dip in the power level (30 nsec is the delay time of the photomultiplier to convert the energy of incident photons into electrical signals) implying a causal relation between the absorption of power and the acceleration of electrons. Figure 3d is an oscilloscope trace of the diode voltage and the millimeter power level and figure 3e is a trace of the voltage and the photomultiplier signal. The time scale in figure 3e is 50nsec/div. while in figure 3d it is 20nsec/div.. Examination the two figures reveals that there is a precipitous drop in the power beginning roughly 30nsec after the beam voltage has reached its full value. Correspondingly we find a sudden rise in the Photomultiplier signal at ~ 60nsec after the beam voltage reaches its full value. Both of these striking examples provide

evidence that there exists a causal relationship between the absorption of power and the acceleration of electrons.

II. During the second data run the second optical configuration was used (i.e. two separate optical channels were monitored). Power levels during this second run were much lower and even with no attenuation placed in front of the Schottky detector only weak ~50-100mV power signals were detected. In addition the quest for good energy resolution was frustrated due to the fact that very large horizontal spot widths were found on the quartz plate; even with no undulator field. Both of these phenomenon (i.e. poor power levels and expanded spot size) can be attributed to to a substantial degradation in the quality of the electron beam in the form of a high emittance value for the beam. A high emittance value for the electron beam is fatal to the success of the FEL interaction which generates the radiation required for acceleration and which takes place in the first section of the undulator, since the net energy exchange which must occur between the electron beam and the radiation field relies upon a relatively small energy spread ($\delta\gamma/\gamma$) in the injected beam. Similarly, a large energy spread in the injected electron beam severely limits the focusing ability of the magneto-optic system, which is highly chromatic, as it must be in order to resolve the electrons according to their energies, and causes large spot sizes. Evidence of this large energy spread in the injected beam was also found during the alignment procedure of the electron beam on the axis of the drift tube. To align the electron beam a circular piece of thermal sensitive paper, which fills the cross sectional of the

drift tube, is mounted on a solid graphite cylinder and placed at the downstream end of the drift tube at a position corresponding to the end of the main solenoid. By firing the beam with the guiding field on, the radial position of the electron beam in the undulator can be determined and optimized to coincide with the axis. In general the size of the hole caused by electron striking the paper is ~1.5 mm in diameter, however during the period of this second run the area of the hole increased by a factor of 2. This enlarged area is a telltale sign of a high emittance beam. Fig 4 is a representative diode voltage trace taken during the second data run.

FIG. 4

In figure 4 (time scale 20nsec/div)we notice that indeed the voltage across the diode is constant, however the electrons themselves, which are accelerated by the process of high field emission from the cathode, are sensitive to geometric irregularities (i.e. deformation of the cathode shape and surface roughness) of the graphite tipped cathode which result in a large energy spread in the beam. The graphite tip of the cathode was subsequently reshaped and polished and ultimately replaced entirely in order to improve

beam quality. The lower trace in figure 5a is a sample power profile representative of the low power levels observed during this run, note that the vertical (i.e. power as measured in mV) scale is 1/5 the value of that in figure 3c (i.e. 20mV/div) and still there is only a weak signal. Figures 5b-c are histograms of the power levels observed during the first and second data runs respectively.

FIG. 5

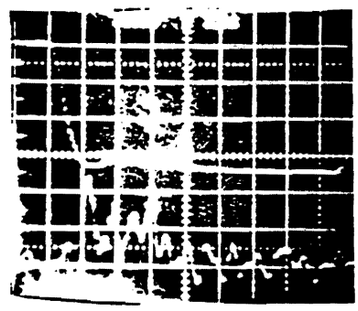

(a)

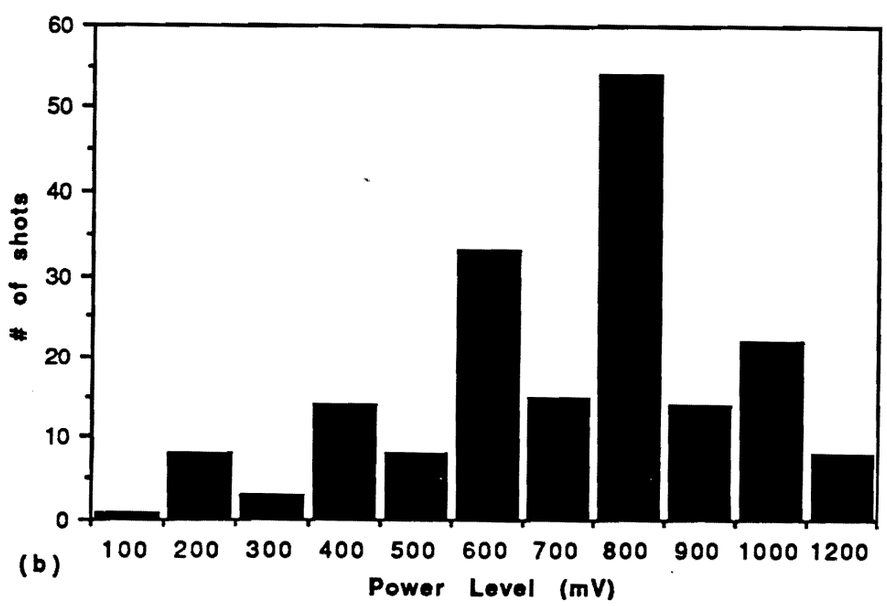

(b)

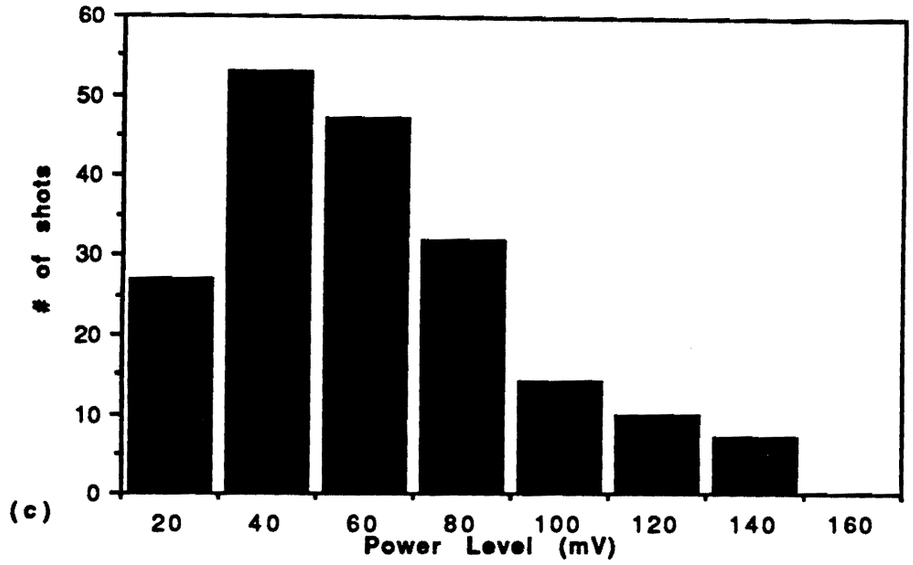

Both photomultiplier channels were monitored on a single oscilloscope trace. Figure 6 is a representative trace taken with $B_{\perp}=0$ in the undulator. The lower trace is the signal corresponding to the injected electrons possessing an energy of 750 keV and the upper trace for those electrons with energy 870 keV. Notice that even when no electrons should be present in the high energy channel a finite signal (exceeding the background x-ray noise) is recorded. The source of this finite signal was understood to be C'erenkov light generated by electrons located in the wings of the spot caused by the electron beam hitting the quartz. The interpretation of the data and the steps taken to account for these anomalies will be dealt with in the next section.(time scale 20nsec/div)

FIG. 6

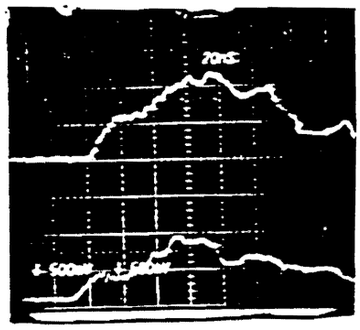

III. The final data run took place using the two channel optical configuration. Output power levels from the IFELA during this run were relatively healthy although they did not reach the same levels encountered during the first data run. Energy resolution of the electrons continued to be a problem as a result of large beam spot sizes, nonetheless satisfactory data was collected during this period after compensation was made for the enlarged spot size.

5.4 DATA SELECTION AND INTERPRETATION

In order for the IFELA to function properly a number of experimental conditions must be satisfied:

1) The diode voltage must remain nearly constant for at least a significant portion of the interaction. Shots where the voltage changed significantly during the shot were discounted since the ramping of the voltage causes an unacceptable spread in the signal frequencies generated in the first section. Also the condition that at least some electrons entering the second section are at the proper resonant phase with respect to the signal as well as the period in the

second section, is hardly satisfied if the beam energy varies appreciably.

2) The two stage IFELA undulator was designed to operate at a particular value of the electron beam energy, hence, even if the injected beam has a constant energy value for the full duration of the interaction, if the energy of the beam is not at the design value less than optimal or no acceleration will result. In both a controlled manner as well as by chance many shots were taken with a constant beam energy that was non-resonant. The data collected for those cases of non-resonance will be presented in the next chapter along with a comparison to the resonant energy data.

3) Finally the output power level must be substantial during any given shot in order for the shot to be considered acceptable. Without sufficient power the potential bucket which traps the electrons is too small and the available energy is inadequate for significant acceleration. It was for this reason that much of the data collected during the second run was discounted due to the poor power production characteristic of that run. Experimental plots of the power absorption as a function of the maximum power level achieved during a given shot will be presented in the next chapter.

A sudden dip in the power levelwhen the electron beam is at the resonant energy value, was taken as evidence of power absorption. The presence of accelerated electrons is evidenced by a rise in the photomultiplier signal following the power dip by a period of time

equal to the response time of the photomultiplier electronics (~30 nsec).

The signal generated by the main group of electrons in the beam at $\gamma \sim 2.4$ is recorded and measurements are made of groups of electrons possessing different energies to determine their populations relative to the main group. The background signal due to x-rays is determined by blocking out the C'erenkov light and observing the phototomultiplier response. This signal due to x-ray noise, as well as the signal generated by electrons located at the edges of spot caused by the main beam, is subtracted from the photomultiplier signal found for electrons at other energies. Figure 7 is a bar graph of the ratio of the number of electrons detected at energy ~1100keV to those with energy ~750keV for the HiB, LoB and $B_{\perp}=0$ modes. The injected beam energy is 750 keV, hence when no undulator field is present there is no means by which the electrons can achieve an energy of 1100keV; thus the 1100keV signal for $B_{\perp}=0$ represents light generated by stray electrons on the edges of the spot. This is the background signal subtracted from the photomultiplier signal for electrons at different energies.

FIG. 7

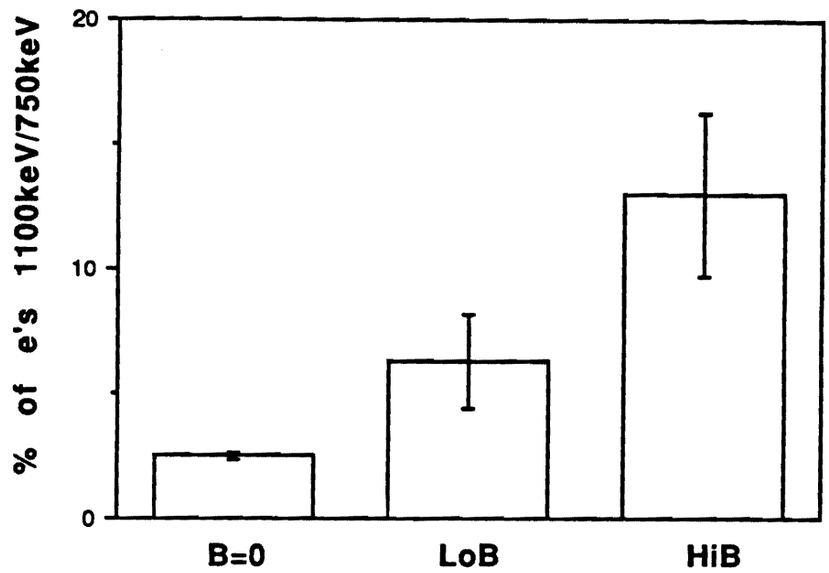

In compiling the final data presented in chapter 6 an average was taken of those shots meeting the previously mentioned criteria. The error bars accompanying the experimental data represent the standard deviation of that data. The theoretical points in the various energy spectra histograms found in chapter 6 represent an energy bin width of $\gamma = \pm .1$ which simulates the experimental bin for the determination of γ.

CHAPTER 6

RESULTS

6.1 RADIATION DATA

The degree of absorption predicted for the IFELA was found numerically to be relatively constant independent of the power level present in the acceleration section of the undulator with the exception of extremely high power levels (i.e. > 100MW) in which case the fraction absorbed drops drastically (i.e. to ~10%). Figure 1 is a plot of the experimental data for the percent absorption as a function of the output power. Note that above a certain minimum power level the percent absorption remains relatively constant. In the data we find a rapid decline in the fraction absorbed as we go to lower power levels (i.e. < 250 mV). Due to the method of beam generation in the Columbia FEL (i.e. high field emission) which is sensitive to the type of material used for the cathode surface as well as the surface roughness (see Chapter 5 Section 2) we attribute the cause for poor power production to a large energy spread

FIG. 1

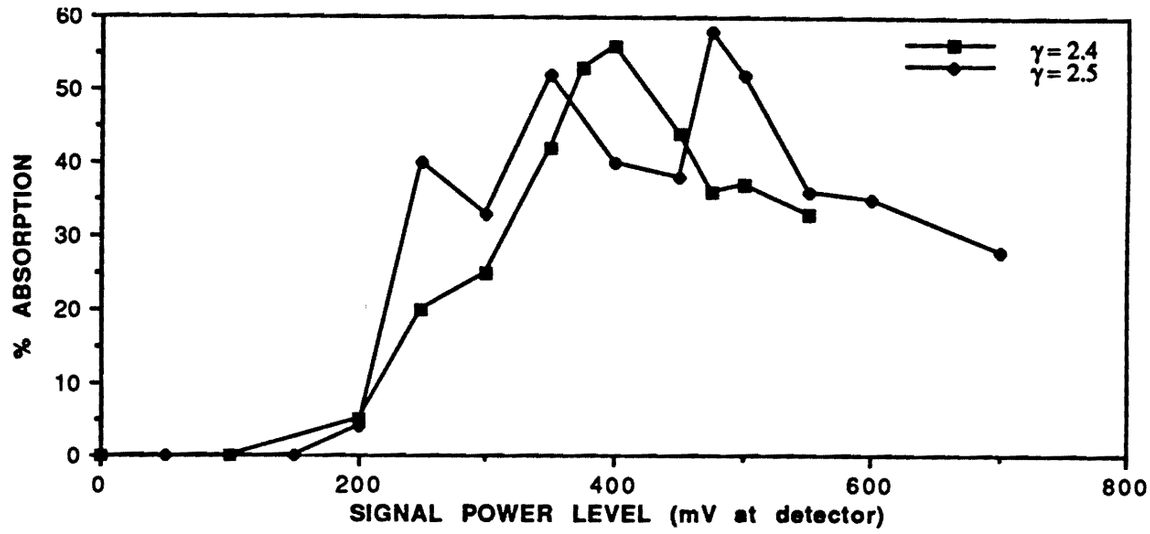

in the injected beam (a "hot beam") entering the undulator. In Chapter 2 Section 2.4 we saw that the effect of a "hot" beam on the FEL interaction is to reduce power production and we found that as the beam grows "hotter" the percent absorption in the second section also drops. Hence, if we recognize that the cause for poor power production in the first section is due to hot beam effects in the injected beam it follows that the radiation absorption in the second undulator section will also be poor.

Throughout the course of data collection the IFELA operated not only at the design energy for the injected beam (i.e γ =2.5) but it also operated, either by design or chance, when the injection beam energy was non-resonant. Figure 2 is a plot of percentage of the signal power transmitted as a function of the injection energy of the electron beam. The manner in which the transmission value is

arrived at is by measuring the transmitted power when a high energy group of electrons is accelerated and dividing that value by the average value of the peak power value immediately prior to and immediately following the drop (as in Chapter 5 Figure 3). The data shown was taken in the case of the higher undulator magnetic field value in the second section of the undulator ($B_\perp$ = 400G) where the theory predicts maximum absorption if the other experimental parameters are correct. According to the data maximum absorption does in fact take place at the design value, however, even at beam energies not on or near resonance we see a finite amount of radiation absorption.

FIG. 2

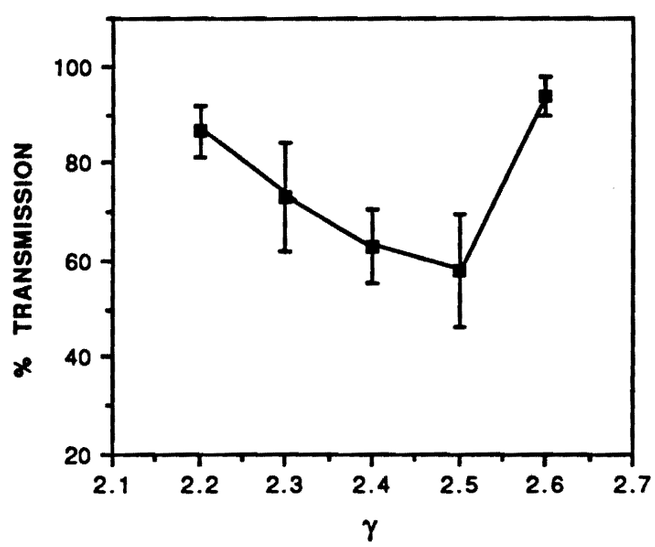

The average amount of absorption that takes place at the design energy value is ~40%. This value is lower than the theoretically

predicted value of ~60% obtained from the simulation. This discrepancy is explained if we remember that the numerical simulation does not include the power generated at the sideband frequencies. This power can constitute a significant portion of the total power, up to 33% [26], thus the experimental value for the absorption does not deviate substantially from the predicted value if one considers that the detector measures power output at the carrier wavelength which is absorbed as well as the sideband wavelengths which is not.

Figure 3 is a plot of the transmission as a function of energy for the case of lower magnetic field in the second section ($B_\perp$ = 250G).

FIG. 3

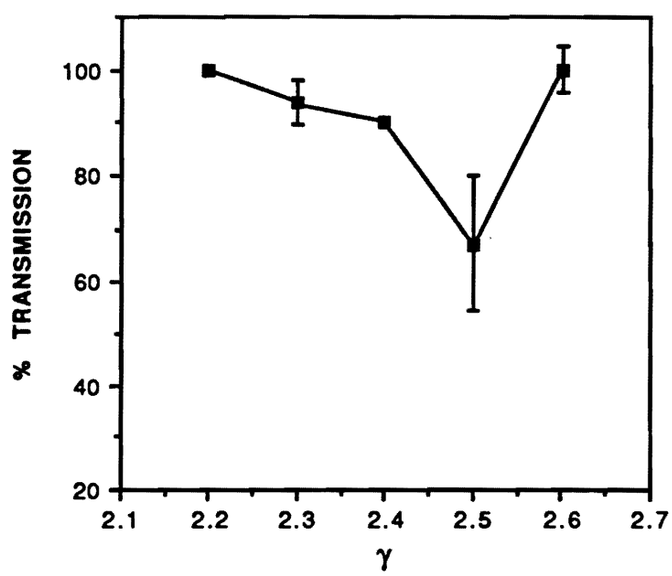

For this case we see that the absorption peak is more pronounced, at the resonant (i.e. design) value, than in the preceding plot. Also the maximum amount of radiation absorption is somewhat (~10%) less than that found in the first case with the higher magnetic field value.

The fact that we observe less absorption in the case of lower magnetic field in the second section is not surprising, since the number of electrons accelerated, and therefore the amount of stimulated absorption, scales with the magnetic field strength in that section.

Regarding the relative sharpness of the absorption peak, the energy spread of the electrons that participate in the acceleration process is governed by the height of the ponderomotive buckets that trap the electrons. The "bucket height" $\Delta\gamma/\gamma$ is proportional to $\sqrt{a_s a_w}$; thus, for the case of lower a_w in the second section the bucket height, and therefore the allowed initial energy spread, for electrons that can be subsequently accelerated is diminished.

In evaluating the results of the radiation data we find evidence of stimulated absorption and, in general, good agreement with the theoretical predictions. In the next section we will examine the data for the energy distribution of the electrons exiting the IFELA.

6.2 ELECTRON ENERGY DATA

Data for the electron energy spectrum for the IFELA was compiled for each individual data run. The data from each run was then combined yielding a final electron energy spectrum for the experiment. Figures 4a-c are the spectra for the first, second and third data runs respectively. These plots represent data taken while the IFELA was in the high magnetic field mode in the second section.

FIG. 4

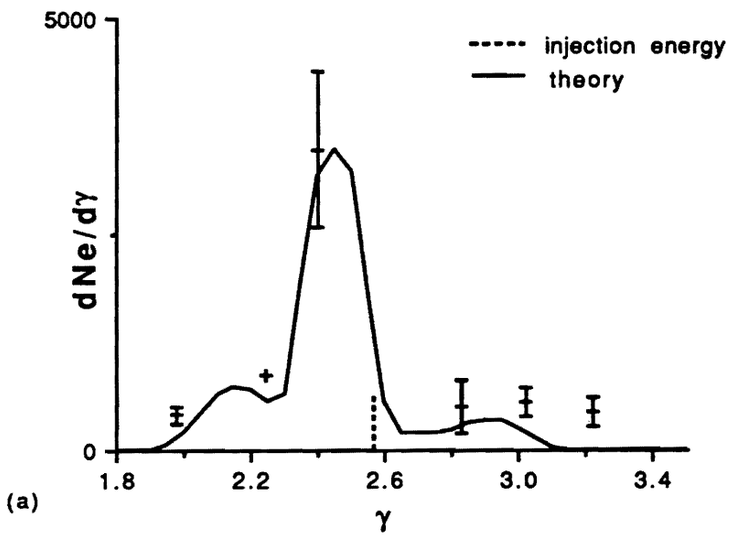

(a)

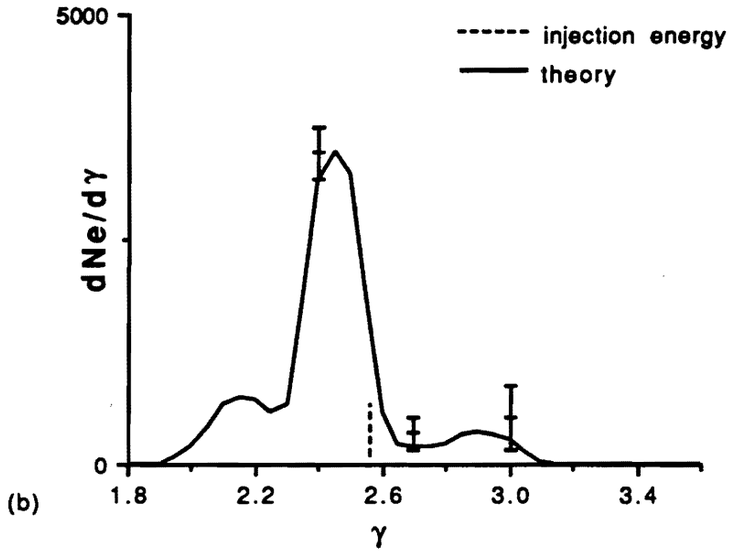

(b)

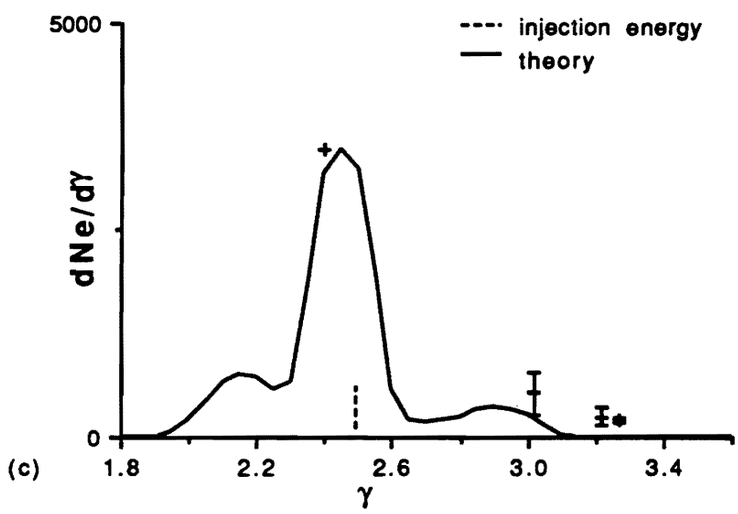

(c)

In all the figures evidence of an energy downshift for the main group of electrons is observed along with evidence of a group of electrons attaining energies substantially higher (i.e. $\gamma \sim 3$) than the injection energy. Figure 5 is a combined plot taken from data collected during all the data runs for the case of high magnetic field.

Included in the plot is the energy spectrum of the injected electrons at the end of the first undulator section prior to entering the accelerator section. We find that the agreement with the theory curve is within the experimental error, the experimental points being somewhat higher consistently for all the spectra. In the experiment some electrons were detected at higher energy values ($\gamma \sim 3.2$) than those predicted by the theory, albeit in very small amounts. The means by which electrons are accelerated to these high energy values remains unexplained by the theory.

FIG. 5

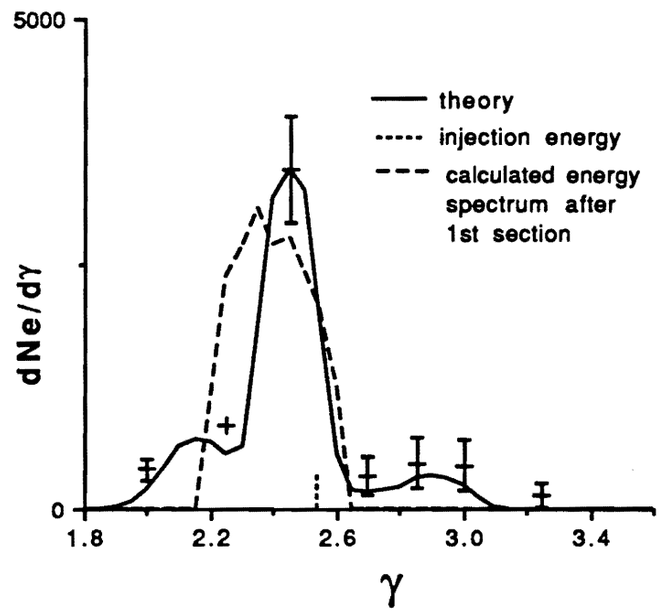

The existence of the "valley" in the energy spectrum between the main group of exiting electrons and the accelerated electrons predicted to occur at $\gamma \sim 2.7$ is supported by the data within the experimental error. Although the predicted depth of the valley is not

verifed conclusively, it is important to note the significant result that fewer electrons are detected at an energy of $\gamma \sim 2.7$ than at $\gamma \sim 3.0$, the data does support the prediction that those electrons exiting the IFELA at energies well above the injection energy are not simply derived from the "wings" of an electron beam with a very large energy spread.

Electrons which are significantly downshifted in energy as a result of the interaction with the IFELA undulator is observed. The theory predicts that the size of the energy downshift for the electrons in the case of the IFELA is greater than the energy downshift found in the case of a conventional FEL and, indeed in viewing the data, electrons are detected at energy values lower than those predicted for electrons exiting from a conventional FEL.

Individual spectra for each data run in the low magnetic field mode were not compiled due to the small amount of data taken while the IFELA was in that mode during any one of the data runs. However, an energy spectrum was compiled for the low field mode from data taken from all the runs. Figure 6 is a plot of the energy spectrum for electrons exiting the IFELA in the case of low transverse magnetic field ($B_{\perp}$=250G) in the second undulator section. The theory predicts that fewer particles will be accelerated to $\gamma \sim 3$ as can be seen from the figure.

FIG. 6

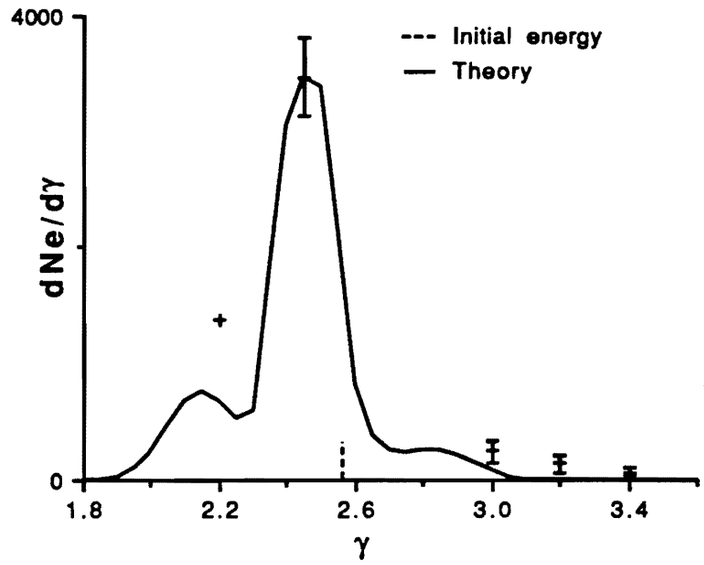

The data shows that, in fact, fewer electrons are detected at higher energies than were detected in the previous case with the higher magnetic field. There is marginal agreement between the theory curve and the data points in the figure. Once again electrons were detected at energies higher than those predicted by the theory and the number of electrons detected at $\gamma \sim 3$ is slightly higher than the predicted value. It should be noted that data collection for this case was not carried out quite as systematically as in the high magnetic field case and hence there was insufficient data to plot points for electrons with $\gamma = 2.4$ -3.0.

Finally, in figure 7 we present a plot of the electron energy spectrum for the case involving an electron beam injected at γ=2.4 (i.e.off resonance) into the IFELA with a high undulator magnetic

field in the second section. This plot, when compared with the other examples, provides a way to judge the sensitivity of the IFELA to the initial conditions of the electron beam. We see from the data that in fact some electrons are still accelerated to $\gamma \sim 2.7$ but there are few electrons at $\gamma \geq 3$ in this case. In figure 2 we saw that a smaller but still significant amount of absorption takes place for the case involving a beam injected at this off-resonant energy. Thus it is not surprising to discover that acceleration does take place in the non-resonant case. The theoretical energy spread for this case shows few or no electrons are accelerated to $\gamma \sim 3$ in contrast to the case of standard injection at the resonant energy.

FIG. 7

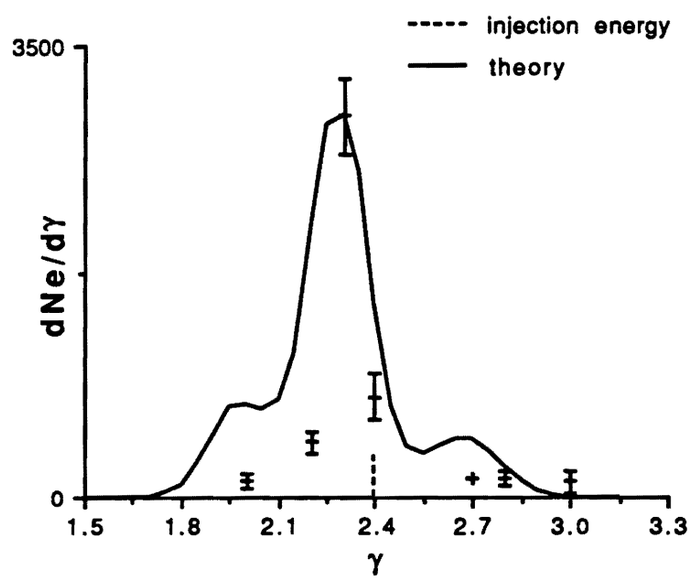

In the off-resonant example some electrons were detected at energies higher than the injection energy. However the more subtle features of the theory curve, such as the existence of a large group of electrons at $\gamma \sim 2.7$ was not found. Unlike the case where the injected beam is at a resonant energy, electrons at $\gamma \sim 3.0$ were detected in very small amounts with the error bars approaching zero; this finding shows that the acceleration is in fact sensitive to the initial energy of the electron beam with a resonant injection energy being necessary to achieve maximum acceleration. Furthermore the data suggests that significantly fewer electrons are accelerated to a γ of 2.7 than predicted by the theory.

In reviewing all the data in this section we find evidence that we have in fact successfully accelerated electrons using the IFEL mechanism present in the IFELA achieving an acceleration gradient of ~7keV/cm using the parameters of our experiment. Furthermore this acceleration appears to be a consequence of the absorption of EM signal power which occurs in the device. Thus we conclude that we have observed the phenomenon of stimulated absorption in our experiment and that the theoretical expectations for electron acceleration have been met in praactice, using a simple undulator designed for that purpose.

CHAPTER 7

AN IFEL ACCELERATOR TEST DEMONSTRATION

7.1 INTRODUCTION

As a result from the IFELA experiment we found that the IFELA was capable of accelerating electrons with an acceleration gradient of ~7keV/cm. While this result in itself is not record setting, it is the first experimental demonstration of electron acceleration using the IFEL mechanism. Numerical studies reveal that if we further optimize the taper in the second undulator section then we can achieve even higher acceleration gradients. FEL theory states that the rate of electron acceleration is governed by the equation**:

$$\frac{d\gamma_i}{dz} = -\frac{a_w a_s k_s}{\gamma_i} \sin\psi_i$$

If we use the relation $k_s \sim 2\gamma^2 k_w$ we can rewrite this equation to yield:

$$\frac{1}{\gamma_i}\frac{d\gamma_i}{dz} = 2a_w a_s k_w \sin\psi_i \text{ or } \frac{1}{L_a} = 2a_w a_s k_w \sin\psi_i$$

**Here and in what follows we neglect the space charge term (i.e. the $\omega_p{}^2$ term) in the energy equation. This is justified since in the high γ cases presented the first term (i.e. α $a_w a_s \gamma$) dominates the energy equation.

Where L_a is the characteristic length of acceleration. We find that the acceleration rate is proportional to the product $a_w a_s$ or in other words the characteristic acceleration length scales as $L_a \sim \frac{1}{a_w a_s}$. Thus, theoretically, if we raise the laser power by a factor of 100 keeping the wavelength constant (i.e. $a_s \propto E_s \propto \sqrt{I_s}$ by a factor of 10) and the strength of the transverse magnetic field on axis by a factor of 10 (i.e. $a_w \propto B_\perp$ by a factor of 10) we can achieve an enhancement of 100× in the acceleration gradient to 700KeV/cm or 70MeV/m. In this chapter we will explore the possibility of achieving acceleration gradients, using an IFEL, that are better than gradients attained using conventional Klystron accelerator technology (i.e. 10-20 Mev/m)[10,39]. The numerical simulation used for this study was developed by Dr. S.Y. Cai, and his many contribution to our undertaking are acknowledged.

7.2 A MODEL FOR AN IFEL ACCELERATOR

The design of the "next" IFEL accelerator test experiment would incorporate a number of features significantly different from those used in the IFELA experiment. As a model for an advanced IFEL we have been guided by the IFEL studies done at Brookhaven National Laboratory[37] where an advanced IFEL accelerator experiment has been planned for late 1992. The following is a list of features that would be present in an advanced version of the IFEL:

1) The electron beam used in our experiment was a high current 1MeV beam. In the construction of an advanced IFEL the injected beam would have a much higher energy value. The initial beam energy in our simulation is 50MeV. The benefits of using a higher energy injection beam for the IFEL are twofold. First, using a higher energy injected beam produces electrons which are accelerated to energies (> 100MeV) that are of real interest in a number of research areas that would benefit from an inexpensive and more compact accelerator technology. Second, if we use the FEL scaling relation mentioned in Chapter 1 (i.e. $\lambda_s=\lambda_w/2\gamma^2(1+a_w^2)$) we find that the resonant optical wavelength for such a device will be within the range of conventional lasers which are capable of producing high intensity laser beams (i.e. $\sim 10^{11}$ W/cm^2 where $k_s \sim 6000$ cm^{-1}($\lambda_s \sim 10\mu$) and $a_s \sim 10^{-1}$). This can be done using an undulator period on the order of $\lambda_w \sim 1$cm, thus not requiring an unrealistically small value for λ_w.

2) There is no need to generate signal power in the undulator itself when using an external laser. If the optical beam of the laser has a gaussian profile then the undulator length can be set to equal two Rayleigh lengths (i.e. undulator length= $2 \times Z_r$, where $Z_r = \pi w_o^2/\lambda_s$ and w_o is the value of the beam waist); this will provide for a high laser intensity on the axis for the length of the undulator. Another method proposed to confine the optical beam as it propagates down the undulator (not used in our simulation) is to employ an optical waveguide for the length of the interaction region. The walls of the

optical waveguide would be coated with a suitable dielectric material so that the optical power loss in the waveguide could be minimal[38] (i.e. 10^{-5} dB/m). The laser we choose for our simulation is a CO_2 laser since the wavelength of the output radiation (λ_s=10.6 μm) can be made resonant given the beam energy and the other experimental parameters; also high power CO_2 lasers are readily available and thus no new laser technology would be required.

3) The undulator design would resemble the second section of the IFELA undulator. Namely it would have a reverse taper which is designed to maintain the electron beam/light signal acceleration resonance relation, as the beam energy grows, for the length of the undulator. Preceding the reverse tapered section an initial undulator section having a constant period is used. The purpose of this constant period section would not be to produce radiation (i.e. λ_w is not resonant for signal amplification) as is the case in the IFELA, rather it would serve to bunch the electron beam before entering the accelerator section. This allows the electrons to be confined in the ponderomotive buckets before entering the tapered section resulting in a larger number of accelerated electrons. The transverse magnetic field on the axis of the undulator would be set to a value appreciably higher than that used in our experiment since the acceleration rate is directly proportional to $a_w(=eB_\perp/k_w mc^2)$. Increasing a_w also serves to increase the bucket height of the ponderomotive wells ($\Delta\gamma/\gamma \sim \sqrt{a_w a_s}$) and thus increase the number of electrons participating in the acceleration process. In the study which follows a simple linear taper

is used, however more detailed studies will involve nonlinear taper functions which can further optimize the acceleration gradient.

7.3 SIMULATION RESULTS

Table 1 shows the experimental parameters used in the advanced IFEL simulation using a gaussian beam profile for the input laser beam:

TABLE 1

Undulator period	λ_w=2.48 cm
Length of constant section	25 cm
Undulator taper	$\frac{d\lambda_w}{dz} = 2\pi \times .0122 \approx .0767$
Length of tapered section	75 cm
Transverse magnetic field	$B_{\perp(max)}$=1.5 T (a_w=2.61)
Laser wavelength	λ_s=10 μm
Initial laser power	8×10^{10} W
Laser beam waist	w_o =.119 cm
Laser Intensity at beam waist	1.79×10^{12} W/cm^2
Rayleigh Range	Z_r =44.5 cm
Electron beam radius	r_b=.03 cm

In figure 1 we see the resultant electron energy spectrum from the numerical simulation done using the parameters in Table 1.

FIG. 1

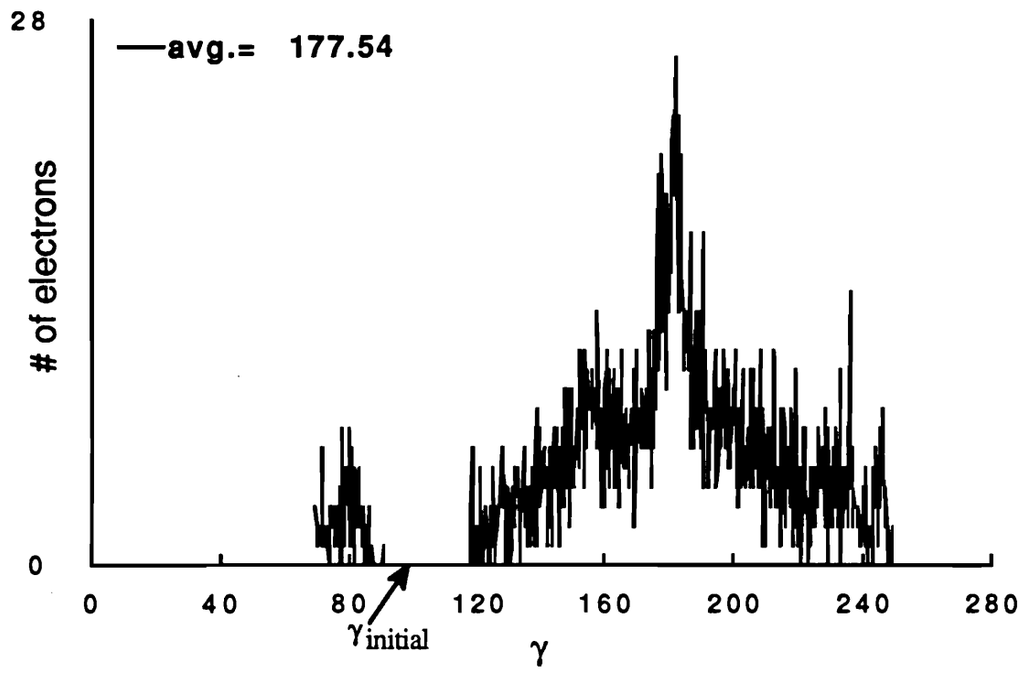

We can see from the figure that most of the electrons (>75%) are accelerated to substantially higher energies (e.g. ~95 MeV). Moreover we find that a peak in the number of accelerated electrons exists at γ ~ 190. However some features of this energy spectrum are less than ideal. Firstly, a large number of particles do not participate in the acceleration process and as a result we find them at the low energy end of the spectrum. Secondly, the group of electrons which is accelerated has a large spread in the electron energy distribution (with the exception of electrons at γ=190) ranging from γ =120-240. To increase the fraction of particles participating in the acceleration process as well as to reduce the energy spread of the accelerated particles we must look at the manner in which the electrons are initially trapped in their ponderomotive potential wells. In the

simulation the input laser power is very large (i.e. $a_s=10^{-1}$) as is also the value of a_w and therefore the bucket height ($\Delta\gamma/\gamma \sim \sqrt{a_w a_s}$) which determines the allowable energy range for the participating electrons is very large. This large energy range in the phase space of the electrons means that as the center of the potential well rises, at the end of the constant period section of the undulator, those electrons entering the tapered section with low energy values will not participate in the interaction. Also the resulting energy spread of the accelerated electrons is large owing to the large energy spread in the electrons entering the tapered section. To remedy this situation we should inject the electrons colinearly with a lower intensity laser (10^{10}W/cm^2) into the constant period section thereby reducing the energy spread $\Delta\gamma/\gamma$ of the electrons as they enter the second section. This can be done either using a gaussian beam in free space or using an optical waveguide extending the length of the constant period section. A second optical beam with a much higher intensity ($\sim 1.8\times10^{12}$ W/cm^2) at its own beam waist should be focused such that its intensity would become appreciable at the start of the tapered section. Figure 2 is the resultant electron energy spectrum if the laser power is increased abruptly by a factor of 100, at the beginning of the tapered section, all other parameters are identical to those listed in table 1.

FIG. 2

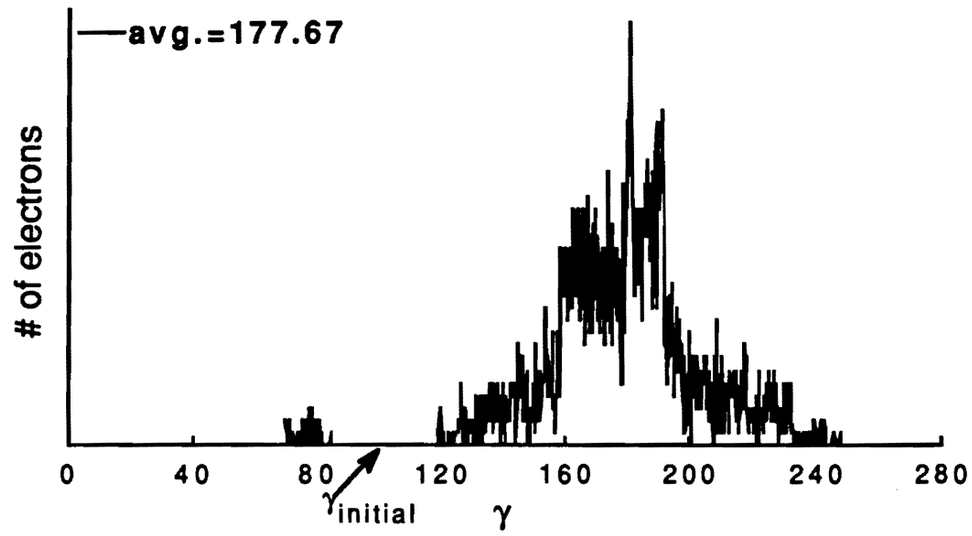

Clearly, more electrons are accelerated in this case (i.e. > 98%) and we also find that the accelerated electrons are more localized in energy near γ=190. We can thus conclude that it is highly desirable to incorporate this feature of increasing the laser intensity on the axis at the start of the acceleration section of the IFEL. If, in addition, a more intricate function for the taper is included into the design of the undulator the energy spread of the accelerated electrons can be reduced even further.

In the two preceeding examples the on-axis light intensity varies significantly (i.e. by a factor of 2) as the electrons traverse the undulator due to the gaussian profile of the laser beam. By enlarging the beam waist such that the Rayliegh range becomes much larger than the undulator length we can keep the on-axis intensity relatively constant (the value at the waist being 4-5% greater than

the value at the ends of the undulator) for the length of the undulator. Figure 3 is the simulation result for the case where the laser power is kept constant at $\sim 2 \times 10^{11}$ W the beam waist is set at .5 cm and due to the new value of a_s the tapering parameter is changed to a new value $\frac{d\lambda}{dz} = .125$, all other system parameters are the same as those presented in table 1 of this chapter.

FIG. 3

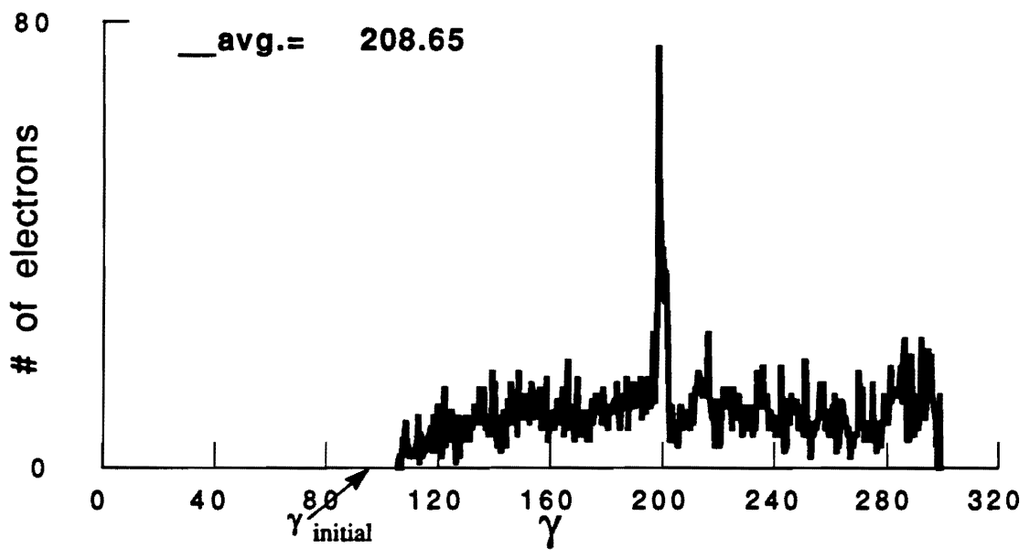

We find in this case that a significant number of electrons are accelerated to a relatively well defined energy at $\gamma \sim 200$. Nonetheless we find here as before that electrons can still be found distributed over a wide range of energies.

7.4 CONCLUSIONS

The simulation results presented in this chapter suggest that the IFEL mechanism is a viable means of electron acceleration using technologies that already exist. The acceleration gradient achieved in the simulation for the IFEL is on the order of 45-70MeV/m, which is attractive and in fact exceeds the acceleration rates achieved using conventional linac technology[39]. If the energy of the electrons approaches a few GeV the losses due to synchrotron radiation become significant and this will place an upper limit on the possible electron energies that can be achieved using the IFEL. (Methods for surpassing this upper limit on the energy have been proposed[40] which involve the simultaneous tapering of the undulator period as well as the transverse magnetic field $B_\perp$ in the undulator in such a way as to significantly reduce synchrotron losses.)

REFERENCES

1. L.R. Elias, W.M. Fairbank, J.M.J Madey, H.A. Schwettman and T.I. Smith, *Phys. Rev. Lett.* vol.36 p710 (1976)

2. D.A.G. Deacon, L.R. Elias, J.M.J Madey, G.J. Ramian, H.A. Schwettman, and T.I. Smith, *Phys. Rev. Lett.*, vol. 38 p.892(1977)

3. H. Motz and M. Nakamura, *Annals of Physics*, vol. 7,p. 84 (1959)

4. R.B. Palmer, *J. Appl. Phys.*, vol. 43, p. 3014, (1972)

5. E.B. Courant, C. Pelligrini, and W. Zackowitz, *Phys. Rev. A*, vol. 32. No. 5 p. 2813, (1985)

6. W.B. Colson and S.K. Ride *Appl. Phys.* vol. 20, p.61 (1979)

7. P. Sprangle and C.M. Tang, *IEEE Trans Nuc. Sci.* NS-28 p. 3346 (1981)

8. T.C. Marshall and I. Wernick, Nuc. *Instr. and Meth. in Phys. Research*, A304 (1992)

9. T.C. Marshall,S.Y. Cai, A. Bhatacharjee, Y.P. Chou and I. Wernick, *Nuc. Instr. and Meth. in Phys. Research*, A304 (1991)

10. SLC-design Report, SLAC report #229, (1980)

11. For a comprehensive review of laser accelerator shemes see: Laser Acceleration of Particles, Proceedings of the Workshop on the laser acceleration of Particles edited by P.J. Channel (AIP, New York, 1982)

12. For a discussion of the Plasma Beat Wave Accelerator see; T. Tajima and J.M. Dawson, *Phys. Rev. Lett.* 43, p. 267 (1979)

13. For a discussion of the Laser-Plasma Wakefield see; P. Sprangle, Appl. Phys. Lett. vol. 53, p.2146 (1988)

14. For a discussion of the Laser Beat Wave Accelerator See Ref. 7

15. T.C Marshall, Free Electron Lasers, Macmillan, New York, (1985)

16. F.A Hopf, P, Meystre, M.O. Scully and W.H. Louisell, *Phys. Rev. Lett.* vol. 37 p. 1215 (1976)

17. W.B. Colson, *Phys Quant Elect.*, vol. 5, p. 152, (1977)

18. C.A. Brau and R.K. Cooper, *Phys. Quant. Elect.*,vol. 7, p. 647, (1980)

19. F.G. YEE, T.C. Marshall and S.P. Schlesinger IEEE Transactions on Plasma Science, vol. 16, No. 2, p. 162,(1988)

20. W.B. Colson and R.A. Freedman, *Phys Rev. A*, vol. 27, p. 1399, (1983)

21. N.M Kroll, P.L. Morton, M.N. Rosenbluth, *IEEE J. Quant. Elect.*, vol. QE17, p. 1436, (1981)

22. S.Y. Cai, Doctoral Thesis, Columbia Univ. (1989)

23. T. Stenholm and A. Bambini, *IEEE J. of Quant. Elect.*, vol. QE17, p.1363 (1981)

24. W.B. Colson, *Phys. Lett. 63A*, 190 (1977)

25. N.M Kroll, P.L. Morton, M.N. Rosenbluth, *Physics of Quantum Electronics*, vol. 5, Addison Wesley, Reading, MA, p.81 (1980)

26. Leon Lapidus and John F. Seinfeld, in *Numerical Solution of Ordinary Differential Equations*, Academic Free Press New York and London, p.189 (1971)

27. J. Masud, T.C. Marshall, S.P. Schlesinger and F.G. Yee,*IEEE J. of Quant. Elect.*, vol. 23, No. 9, p.1594 (1987)

28. J.W. Dodd, Doctoral Thesis, Columbia Univ. (1990)

29. P.C. Magnusson, Transmission Lines and Wave Propagation, Allyn and Bacon, Boston, (1970)

30. The electron trajectory program is based on the SLAC electron trajectory code originally written by W.B. Herrmannsfeldt. For A more detailed reference of the design used here, see R.H. Jackson, S.H.

Gold, R.K. Parker, P.C. Efthimion,, V.L. Granatstien, M Herendon, A.K. Kinkead, J.E. Kosakowiski, and T.J.T. Kwan, in " Design and operation of collective millimeter-wave free electron laser", *IEEE J. of Quant. Elect.* , QE19, p.346 (1983)

31. H.P. Freund, S. Johnston, and P.Sprangle, *J. of Quant. Elect.* , QE19, p.322 (1983)

32. R.H. Pantell, J. Feinstein and A.H. Ho, *Nuc. Instr. and Meth. in Phys. Research*, A296, p.638 (1990)

33. J. Masud Doctoral Thesis, Columbia University, (1987)

34. B.M. Kincaid, *J. Appl. Phys.*, vol. 48, p. 2684 (1977)

35. TRANSPORT© written by F. Rothacker(SLAC) and C. Iselin(CERN) et al., copies may be obtained by writing; The Reports Office SLAC P.O. Box 4349, Stanford, CA 94305 (Ref.# SLAC-91)

36. B. Kulke, M.J. Burnsard and T.J. Orzechowski, LLNL report UCRL-95598

37. Brookhaven Informal Report CAP#81-ATF-91P, form Accelerator Test Facility users meeting, p.153 (1991)

38. W Zackowitz, *J. Appl. Phys.*, vol. 55, p. 3421 (1984)

39. H.Piel, Recent progress in RF superconductivity

40. C. Pelligrini and R. Campisi, in Physics of High Energy Particles Accelerators, Proceedings of Lectures given at the National Summer School on High Energy Particle Accelerators, edited by M. Month p. 1058 (AIP, New York, 1983)